Journal of Applied Fluid Mechanics, Vol. 17, No. 1, pp. 116-135, 2024.
Available online at www.jafmonline.net, ISSN 1735-3572, EISSN 1735-3645.
https://doi.org/10.47176/jafm.17.1.2062

Numerical Study on Aerodynamic Characteristics of Tail-stabilized Projectile with Asymmetrical Diversion Groove

A. A. Luo[1], Q. K. Xiao[1,2], X. Liu[2†], J. C. Guo[3] and Y. H. Zhang[1]

[1] *School of Mechatronic Engineering, Xi ' an Technological University, Xi'an, Shaanxi, 710021, China*
[2] *School of Electronic Information Engineering, Xi'an Technological University, Xi'an, Shaanxi, 710021, China*
[3] *School of Opto-electronical Engineering, Xi'an Technological University, Xi'an, Shaanxi, 710021, China*

†*Corresponding Author Email: lxing@xatu.edu.cn*

ABSTRACT

A surface diversion groove with a specific geometry and position can influence the laminar flow characteristics of a projectile, which may affect the flight trajectory of an aircraft. The asymmetric flow field around the projectile can be induced by the diversion groove, which can produce an obvious aerodynamic force and moment at the projectile nose for trajectory correction. This study applied a diversion groove structure to the nose of tail-stabilized projectiles to investigate its impact on the aerodynamic characteristics of the projectile. The mathematical expressions for the aerodynamic force and aerodynamic coefficient were established theoretically. The change in the aerodynamic coefficient as a function of the phase angle of the diversion groove was determined. A parametric simulation was employed to investigate how the diversion groove affects the aerodynamic attributes of the projectile across various Mach numbers and angles of attack. The simulation results are consistent with the variation trends of aerodynamic forces and moments with respect to the phase angle of the diverter groove, as predicted by the static mathematical model. These findings demonstrate that the variation trends of the lift coefficient and pitching moment coefficient with respect to the angle β approximate a cosine function. Meanwhile, the variation trends of the yaw force coefficient and yaw moment coefficient with respect to the angle β approximate a sine function. The tail-stabilized projectile with asymmetrical diversion groove achieved a reduction of 1.2% in drag coefficient compared with that of the canard rudder corrective projectile, while the lift coefficient and pitch moment coefficient were increased by 6.4% and 16%, respectively, in the subsonic regime. The static margin of the projectile ranging from 13% to 16%. This study offers valuable insights for the design of corrective structures with diversion grooves and trajectory control.

Article History

Received June 6, 2023
Revised August 27, 2023
Accepted September 25, 2023
Available online November 1, 2023

Keywords:

Diversion groove
Asymmetric nose
Two-dimensional correction
Ballistic correction projectile
CFD

1. INTRODUCTION

The complex and dynamic environment of modern warfare necessitates a shift from traditional ammunition with low precision and large dispersion to those with high guidance precision for precise attacks and efficient target damage (Hooker, 2005). An ideal way to modernize armaments and minimize their cost is to analyze the actual use deficiencies of active weapons and make subsequent improvements based on the existing structures (Yin et al., 2018). Recently, the two-dimensional trajectory correction technology has been gradually studied and applied (Massey & Flick, 2007; Massey et al., 2008; Vatsa et al., 2014). Here, the canard rudder correction is the most used correction mechanism, which mainly involves adjusting the aerodynamic characteristics of the projectile through the canard rudder, accomplishing the correction objective (Hamel & Gagnon 2011). This correction mechanism is typically used for large-caliber supersonic spinning artillery shells, and the main factors affecting its correction effect are the canard shape and aerodynamic layout of the rudder plate (Wang et al., 2015). However, the canard rudder correction mechanism has shortcomings, such as the large size of the rudder, its high cost, and its poor resistance to high overload. Therefore, it is crucial to design a two-dimensional mechanism with a simple structure, low cost, high stability, and good reliability.

The asymmetric flow field generated by the fluid around the forebody of the projectile, can change the pressure distribution on the projectile nose (Ericsson, 1993), inducing yaw in the projectile. The generation of an asymmetric flow field depends on several factors, such as the nose shape, surface roughness, and the elongated ratio of the projectile (Bernhardt, 2000). Current research primarily aims to exploit the unique structure of the projectile nose to induce an asymmetric flow field, achieving two-dimensional trajectory correction.

In the 1950s, Goddard (1952) proposed movable nose and tail structures for controlling rocket vehicles under different atmospheric conditions. However, because of the lack of in-depth technical research at the time, the design concept had a poor anti-overload ability and low reliability in practical applications. Inspired by this structural design, Thompson (1981) first proposed the use of a deflectable nose mechanism for tube-launched weapons. Then, many wind tunnel tests (Stutts & Barrett 1998; Landers et al., 2003; Marshall, 2005) and computational fluid dynamics analyses (Vaughn & Auman 2002; 2003) were performed to investigate the aerodynamic attributes of the deflector nose missile. These efforts have aimed to investigate whether the asymmetric flow field can be used to control the flight course of the missile. To investigate the aerodynamic differences between a deflectable nose and a canard rudder control mechanism, Landers & Auman (2001) conducted wind tunnel experiments under supersonic conditions. They found that the deflectable nose mechanism can significantly enhance control efficiency and minimize the air resistance of the projectile. Zhang et al. (2014, 2015) conducted wind tunnel tests on deflectable nose projectiles under subsonic conditions to examine the impact of the deflectable nose mechanism on the aerodynamic attributes of the projectile. Sharma et al. (2015) studied a missile model using both simulations and experiments. A comprehensive analysis of the simulation results and experimental data, showed that the deflectable nose cone considerably affected the flow field on the leeward side of the missile. Ren et al. (2019) conducted wind tunnel tests on a deflectable nose projectile model: implementing a correction of the projectile nose at the peak of its trajectory increased the maximum range by 5.76%. Extensive research findings have shown that the control force generated by nose deflection is positively correlated with the Mach number. Therefore, this method is mainly applied to the control of supersonic or hypersonic missiles. For tail-stabilized projectiles, the flight velocity during trajectory correction typically ranges from 0.8 Ma to 1.2 Ma. Therefore, in the subsonic and transonic ranges, it is difficult for the nose deflection mechanism to achieve optimal correction effectiveness.

In the field of projectile control under transonic and subsonic conditions, Richardson (1948), May (1952, 1975), and Waugh and Stubtad (1975) studied the aerodynamic states of projectiles with different nose shapes (plane, cone, sphere, and dome). Building on these works, Shi et al. (2019, 2020) proposed the structure of an asymmetric nose projectile body with a cutting angle and performed corresponding experiments. The results showed that the air cavity formed around the asymmetric nose projectile was also asymmetric, and the trajectory deflected when the projectile entered the water. Thus, the asymmetrical nose shape provides a relatively stable yaw force for the projectile. Wang et al. (2021) proposed an asymmetric nose structure for an autonomous underwater vehicle (AUV) and developed a numerical model based on the volume of fluid method to study the high-speed water entry cavity and trajectory characteristics of the AUV. These findings provide a strong foundation for developing missiles and torpedoes.

Robarge et al. (2004) considered the groove structure in airfoil research and found that a groove with a specific geometry and position effectively controls fluid separation. In their computational fluid dynamics simulation, Seo and Hong (2016) investigated the impact of the groove structure on airfoil performance. They found that carefully selecting the size and location of grooves considerably improved the lift−drag ratio, achieving an airfoil performance enhancement of 15.3%. Wu et al. (2019) designed groove structures with different parameters on airfoil blades to investigate the variations in turbulence drag. Within a certain range of groove dimensions, the results indicated that the groove structure effectively mitigates viscous drag. However, a larger groove size can cause increased drag, whereas a well-designed arrangement of groove structures is crucial for modifying aerodynamic forces. Thus, arranging the groove at the trailing edge of the airfoil is not recommended. Liu et al. (2020) conducted a comprehensive numerical simulation analysis to investigate the impact of a surface groove structure on the aerodynamic attributes of the NACA 4415 airfoil. The findings demonstrated that for a groove depth ratio of h/w=1.2−1.5, the rectangular groove exhibited notably superior aerodynamic attributes compared to those of the arc groove. Xu et al. (2022) investigated the impact of various bionic groove shapes on the aerodynamic attributes of multi-wing centrifugal fans, identifying why the bionic groove influences aerodynamic characteristics. The strategic incorporation of wing structure enables an effective control over vortex behavior and alters the flow characteristics of the boundary layer.

As indicated by the review above, various projectile nose structures have been studied to induce asymmetric flow fields for trajectory correction. However, limited research attention has been paid to developing correction mechanisms suitable for tail-stabilized projectiles that operate at subsonic or transonic speeds. Groove structures have demonstrated certain advantages in altering aerodynamic characteristics and have achieved substantial results in fields such as aircraft airfoils and turbine blades. Mariotti et al. (2017) successfully controlled the aerodynamic characteristics of an axisymmetric blunt body by incorporating transverse grooves with specific shapes at the rear. However, no research has investigated the application of a trench structure in the field of trajectory control. Therefore, this study placed the diversion groove in an asymmetrical arrangement at the nose of the projectile to induce asymmetric aerodynamic forces, providing corrective forces for tail-stabilized projectiles in the subsonic and transonic ranges. The variation

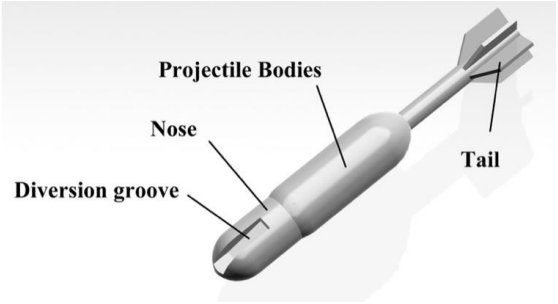

(a) Simplified three-dimensional drawing of asymmetric nose projectile

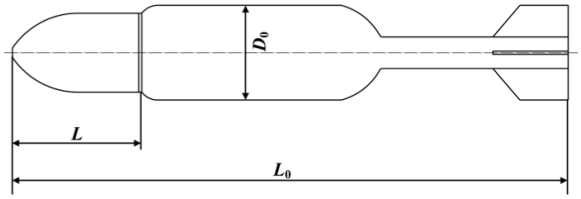

(b) Schematic of projectile with basic dimensions

Fig. 1 Diagram of projectile model

trend of the projectile's aerodynamic coefficients with respect to the diversion groove phase angle was determined theoretically. A numerical simulation was conducted on the projectile model within a predefined flow field, yielding the variations of the projectile's aerodynamic force and coefficient with respect to the phase angle of the groove. This analysis was performed under different Mach numbers and angles of attack. The simulation results were consistent with the variation trends of aerodynamic forces and moments with respect to the phase angle of the diverter groove, as predicted by the static mathematical model. Understanding the variation law of the aerodynamic coefficients of projectiles helps to establish the trajectory control equation and lays a foundation for achieving two-dimensional trajectory correction.

2. PROJECTILE MODEL

2.1 Asymmetric nose projectile model

Most projectile models use sharp-nosed or arched geometric shapes, with only a few studies focusing on the dynamics of blunt-nose projectiles. The blunt-nose structure is beneficial for low-Mach flying missiles. Roos (2001) found that the nose air can be evenly distributed when the nose radius is passivated by 20% and lies within an angle of attack range of 0° to 60°. Additionally, blunt-nose projectiles provide more space and better working conditions for radar or infrared seekers. For a subsonic projectile model, a smooth front streamline enhances the aerodynamic force at the front end and reduces atmospheric drag. Meanwhile, rectangular grooves perform better than arc grooves. Because of the intricate design of the asymmetric nose projectile, it is essential to simplify the projectile model. As this study aimed to investigate the relationship between the diversion groove structure and the aerodynamic attributes of the projectile, to eliminate the interference of redundant

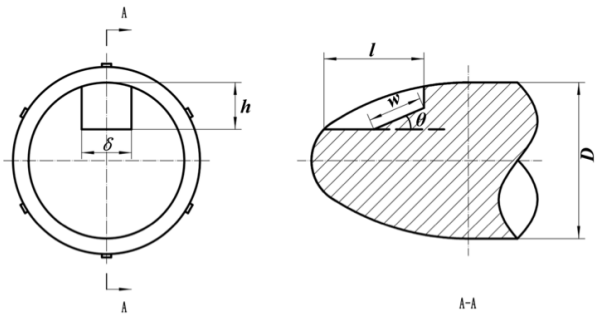

Fig. 2 Diagram of diversion channel

Table 1 Key parameters and symbols

Parameter	Symbol	Numerical value
Projectile length (mm)	L_0	350-380
Projectile diameter (mm)	D_0	60
Nose length (mm)	L	80
Projectile mass (kg)	m	2-2.5
Slope (deg)	θ	10
Slope length (mm)	w	15
Groove length (mm)	l	50
Groove width (mm)	δ	10
Nose radius (mm)	D	50
Angle of attack (deg)	α	-6, -3, 0, 3, 6

factors, only a single diversion groove was retained in the model nose, and the connection structure between the projectile nose and body was omitted. Therefore, we designed a simplified model of an asymmetric nose projectile. The design is based on the blunt-nose projectile model and has a diameter of 60 mm, as shown in Fig. 1.

Ganesan & Esakki (2020) analyzed the aerodynamic effects of different types of grooves in an unmanned amphibious aerial vehicle. Referring to his research results, we illustrate the diversion groove structure designed in this study, as shown in Fig. 2, where D represents the nose diameter. The key geometric parameters of the groove are bevel angle θ, bevel length w, groove length l, groove width δ, and groove height h.

According to the above design description of asymmetric head projectiles, Table 1 provides a summary of the essential parameters for asymmetric nose projectiles.

2.2 Coordinate system

When conducting numerical simulations, establishing a coordinate system relative to the projectile facilitates the analysis of changes in its aerodynamic characteristics. Fixed coordinate systems *Oxyz* and bullet axis coordinate

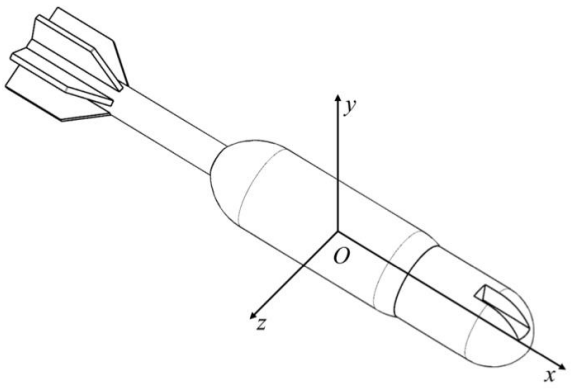

(a) Definition of projectile fixed coordinate system

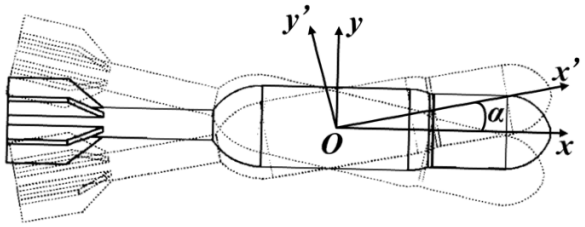

(b) Axis coordinate system and attack angle of projectile α

Fig. 3 Diagram of projectile coordinate system

systems $Ox'y'z'$ are defined on the asymmetric head projectile model, as shown in Fig. 3. Furthermore, α represents the projectile's angle of attack.

3. NUMERICAL METHOD

3.1 Computational Domain

The solution area of the external flow field should reflect the real flow situation of the projectile boundary layer as much as possible. Hence, the flight speed and basic size of the projectile should be fully considered. To ensure accurate calculations and consider the influence of the wake region, the cylindrical outflow field was defined by referring to the mesh division method in airfoil research (Liu et al., 2021). The projectile was positioned at the center of the airflow domain. The fluid inlet was located at a distance of 10 L_0 from the center of the projectile body, while the fluid outlet was positioned at a distance of 15 L_0 from the center, and the radius of the flow field was 20 D_0. The projectile wall was a non-slip boundary condition, as shown in Fig. 4.

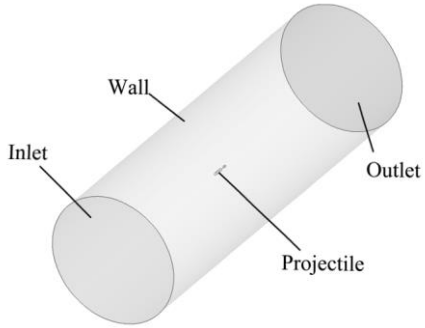

Fig. 4 Outer flow field and projectile position diagram

3.2 Turbulence Models and Governing Equations

Based on the Reynolds-averaged Navier-Stokes (RANS) equations, the governing equations for the fluid can be obtained as follows (Pan et al., 2007):

$$\frac{\partial u_i}{\partial x_i} = 0 \tag{1}$$

$$\frac{\partial}{\partial t}(\rho u_i) + \frac{\partial}{\partial x_i}(\rho u_i u_j) = -\frac{\partial p}{\partial x_i} + \frac{\partial}{\partial x_j}(2\mu S_{ij} - \rho_i \overline{u_j' u'}) \tag{2}$$

where ρ is the fluid density, u is the velocity, p represents the pressure, and μ represents the dynamic viscosity of the fluid. S_{ij} represents the average stress tensor.

Lin and Sarlak (2016) compared the Re_θ-γ, k-k_l-ω, and SST k-ω models. Wauters and DeGroote (2018) compared the three models under low angle of attack conditions. The research findings showed that the SST k-ω model yields a value of 1 for the blending function in the near-wall region, which is equivalent to the standard k-ω model. However, in the far-wall region, the blending function has a value of 0, corresponding to the standard k-ε model. Therefore, this study used the SST k-ω model, which Menter (2009) investigated comprehensively. Compared with the standard k-ω model, the SST k-ω model incorporates a cross-diffusion term and considers the transport process of turbulent shear stress in the definition of turbulent viscosity. The SST k-ω model is commonly used for flow calculations with adverse pressure gradients, airfoil calculations, and transonic calculations, among others. Therefore, in this study, the SST k-ω model is employed. The mathematical expression of the SST k-ω turbulence model is as follows:

$$\frac{\partial k}{\partial t} + u_i \frac{\partial k}{\partial x_i} = \frac{\partial}{\partial x_j}\left[\left(\mu + \frac{\mu_t}{\sigma_k}\right)\frac{\partial k}{\partial x_j}\right] + G_k - \beta' k\omega \tag{3}$$

$$\frac{\partial \omega}{\partial t} + u_i \frac{\partial \omega}{\partial x_i} = \frac{\partial}{\partial x_j}\left[\left(\mu + \frac{\mu_t}{\sigma_\omega}\right)\frac{\partial \omega}{\partial x_j}\right] + G_\omega - \beta'' \omega^2 + D_\omega \tag{4}$$

where t is time; u_i is the mean velocity in the i direction; μ and μ_t represent the dynamic viscosity and turbulent viscosity of the fluid, respectively; σ_k and σ_ω are the turbulent Prandtl constants for turbulent kinetic energy k and dissipation rate ω, respectively; β' and β'' are model constants; and D_ω represents the orthogonal divergence term.

3.3 Mesh Generation

Referring to the simulation methods used by Peng et al. (2017) and Cui et al. (2022) for different projectile models, we divided the computational domain and flow field around the projectile using overset mesh. This method improves computational efficiency and provides a prerequisite for simulating the trajectory of the projectile. The mesh on the projectile surface was locally refined along the normal direction. The total number of grids exceeded 2.4 million. The no-slip wall boundary condition was applied to the surface of the projectile, and the computational domain grid structure is depicted in Fig. 5(a).

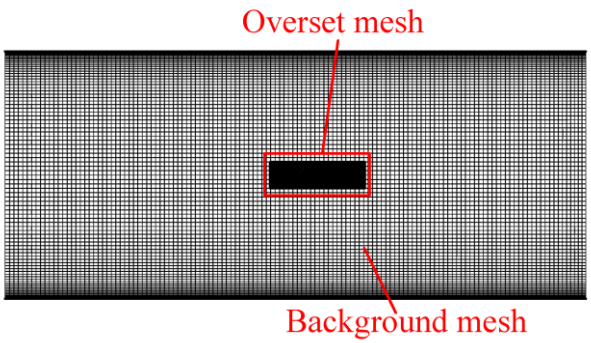

(a) Mesh structure of computational domain

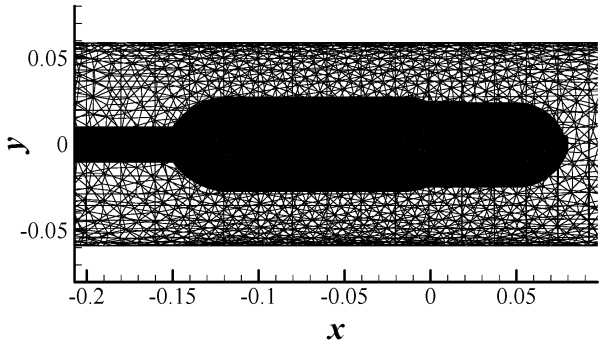

(b) Overset mesh

Fig. 5 Mesh structure of computational domain around projectile

The detailed mesh division of the projectile surface is illustrated in Fig. 5(b).

3.4 Model Validation

To ensure the reliability and accuracy of the numerical simulation results, a validation process was conducted by comparing the simulation results with experimental data. The aerodynamic characteristics of blunt-nose, tail-stabilized projectiles under subsonic conditions have received limited research attention. In this study, the wind tunnel experimental data obtained by Pantelatos & Mathioulakis (2004) on a blunt-nose rotating body model under subsonic conditions were selected as a reference basis. A projectile model with dimensions of D = 127 mm and L = 500 mm was established, as shown in Fig. 6. The experimental conditions were set at 0.3 Ma, α = 10°, and Re = 1.88×10^5.

To ensure computational accuracy, it is necessary to verify the correlation between the numerical results and the number of grid cells. The blunt-nose model and its

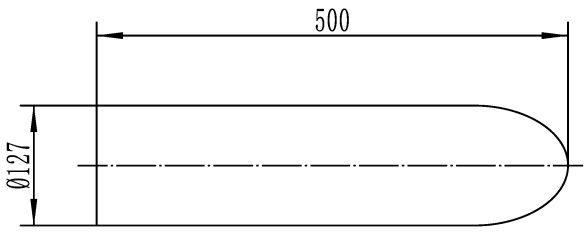

Fig. 6 Blunt axisymmetric model

Table 2 Results of grid independency test

Mesh quantity	Drag coefficient
1,636,356	0.17637
2,459,833	0.17834
2,748,926	0.17856
3,080,235	0.17863

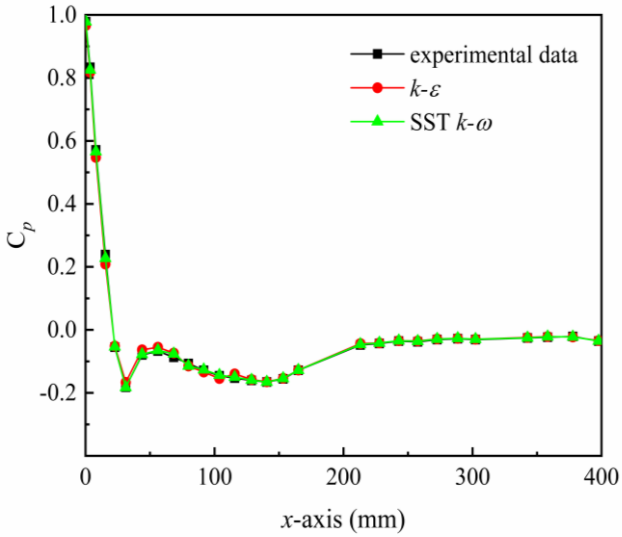

Fig. 7 Pressure distribution of projectile axis obtained by different numerical models

computational domain were divided into four grid densities. The total number of grids gradually increased from 1,636,356 to 3,280,235. The blunt-body model with different grid densities was computed using the same numerical method. Table 2 shows the drag coefficient of the blunt-body model at different grid densities. The verification results showed that the drag coefficient remained relatively stable when the total number of grids exceeded 2,459,833. Considering computational workload and accuracy, we recommend to use a total grid number of at least 2,500,000 when conducting simulations with the chosen computational domain and numerical model.

Figure 7 compares the experimental data of the axial pressure coefficient with the results obtained using the k-ε and SST k-ω models. Both models accurately predicted the axial pressure distribution on the blunt body. They mainly differed as the SST k-ω model performed better than the k-ε model in predicting the results near the head of the blunt body, while the values of both models were relatively consistent in the rear portion of the blunt body. The axial pressure distribution is illustrated in Fig. 7. Compared with the experimental data under the same conditions, the numerical curve of the SST k-ω model shows a consistent trend with that of the experimental curve. This phenomenon indicates that the proposed numerical calculation method accurately reflects the aerodynamic characteristics of the blunt-nose projectile.

Table 3 Simulation data of conventional blunt-nose projectile model

Mach number	Angle of attack (deg)	Drag force F_{x0} (N)	Lift force F_{y0} (N)	Yaw force F_{z0} (N)	Drag coefficient C_{x0}	Lift coefficient C_{y0}	Yaw force coefficient C_{z0}
0.5Ma	0	6.09	-0.02	-0.03	0.1157	-0.0005	-0.0006
0.8Ma	0	15.02	-0.11	-0.19	0.1113	-0.0008	-0.0014
1Ma	0	23.09	-0.17	-0.31	0.1094	-0.0008	-0.0014
0.8Ma	-3	15.01	-0.25	-0.19	0.1111	-0.0018	-0.0014
0.8Ma	-6	14.67	-0.44	-0.05	0.1087	-0.0032	-0.0003
0.8Ma	3	15.01	0.01	-0.19	0.1112	0.0001	0.0014
0.8Ma	6	14.79	0.18	-0.20	0.1095	0.0013	0.0015

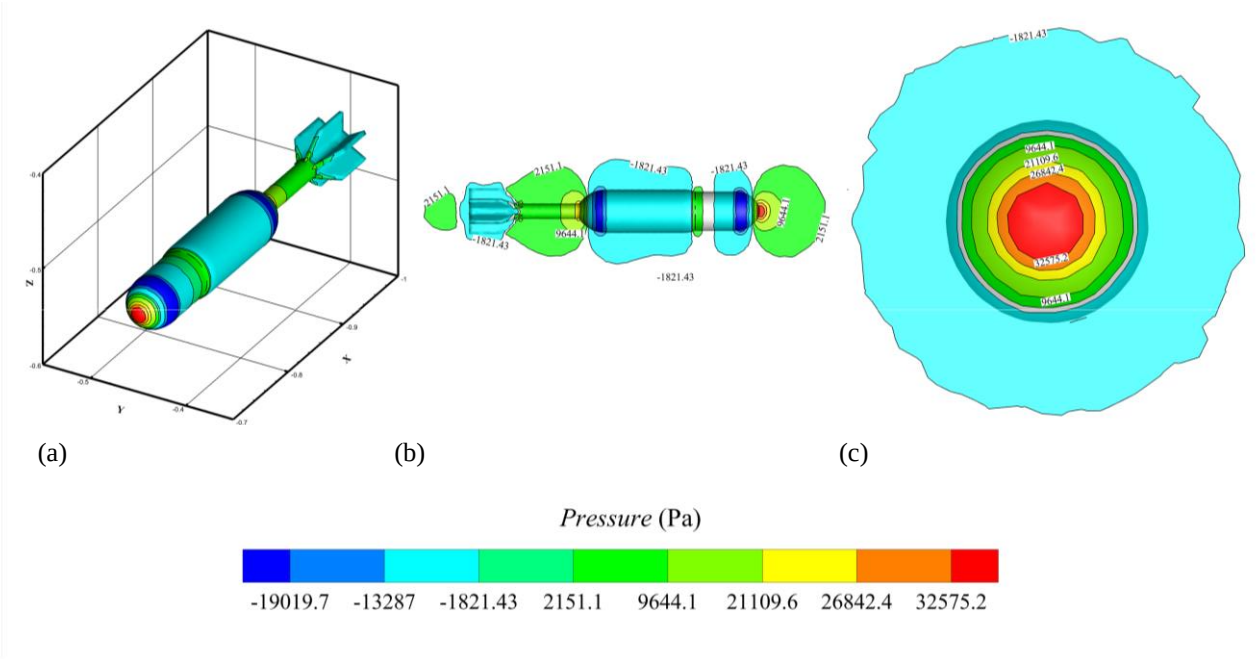

Fig. 8 Pressure distribution on surface and flow field of conventional blunt-nose projectile model

4. ANALYSIS OF ASYMMETRIC FLOW FIELD

4.1 Aerodynamic Characteristics Analysis of Conventional Blunt-Nose Projectile Model

The general blunt-nose projectile model was first simulated under the defined external flow field conditions to provide comparative data for subsequent research. Simulation calculations were used to obtain the drag force F_x, lift force F_y, and yaw force F_z of the conventional blunt-nose projectile model in the fixed coordinate system. Equations (5)−(7) were used to make the aerodynamic force dimensionless, coefficient C_d, lift coefficient C_l, and yaw force coefficient C_z of the model were obtained. The simulation data are presented in Table 3.

$$C_x = \frac{F_x}{0.5\times\rho\times V^2\times S} \tag{5}$$

$$C_y = \frac{F_y}{0.5\times\rho\times V^2\times S} \tag{6}$$

$$C_z = \frac{F_z}{0.5\times\rho\times V^2\times S} \tag{7}$$

where ρ is air density, V is fluid flow rate, and S represents the characteristic area, which corresponds to the largest cross-sectional area of the projectile.

Given 0.8 Ma and 0° angle of attack, the distribution of pressure in the flow field surrounding the conventional blunt-nose projectile model was calculated as illustrated in Fig. 8. Aiming at the center of the projectile as the research object, the curve depicting the distribution of pressure on the surface of the projectile was obtained as shown in Fig. 9. Figure 10 shows the velocity vector distribution in the external flow field surrounding the projectile.

The figures intuitively show that the pressure on the surface of the projectile and the flow field around it maintain a symmetrical distribution. The contact between the projectile's nose and the airflow increases the pressure at the frontal region and decreases the airflow velocity. After the fluid is squeezed, it flows along the boundary layer, and its velocity gradually increases while the pressure decreases. Furthermore, the negative pressure region at the tail of the projectile can induce the airflow to move toward the central axis, thereby enhancing the aerodynamic thrust on the projectile and ultimately increasing the range.

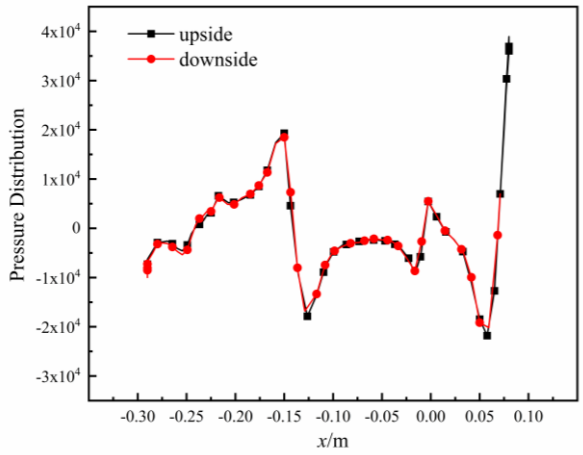

Fig. 9 Pressure distribution on center section of conventional blunt-nose projectile model

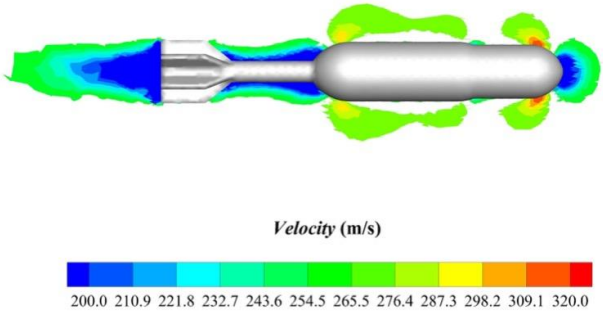

Fig. 10 Velocity vector distribution outside conventional blunt-nose projectile model

4.2 Qualitative Analysis of Asymmetric Flow Field

This analysis focuses on the asymmetric flow field under the conditions of 0.8 Ma and 0° angle of attack. Figure 11 depicts the distribution of surface pressure and the surrounding flow field of the asymmetric nose projectile model. Figure 12 presents a schematic representation of the surface pressure distribution on the center cross-section of the diversion groove. Figure 13 illustrates the distribution of velocities in the external drainage area surrounding the asymmetric nose projectile.

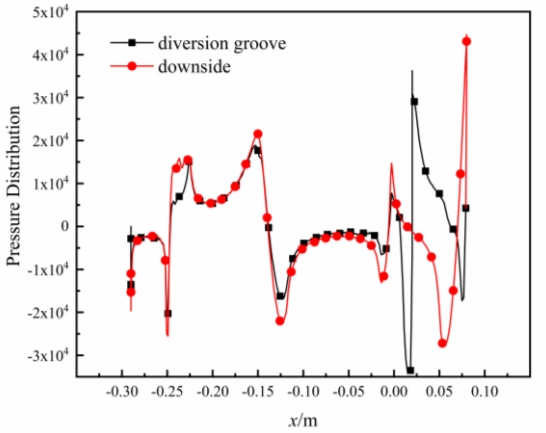

Fig. 12 Pressure distribution on center section of asymmetric nose projectile model

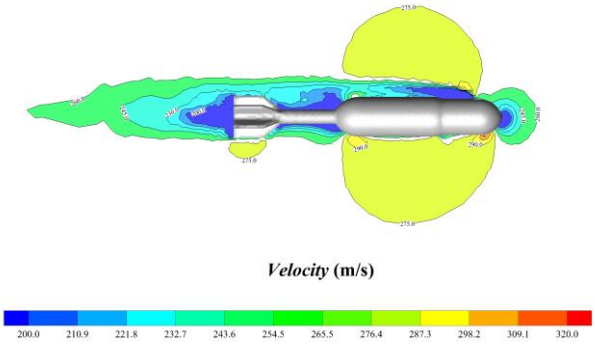

Fig. 13 Velocity vector distribution outside asymmetric nose projectile model

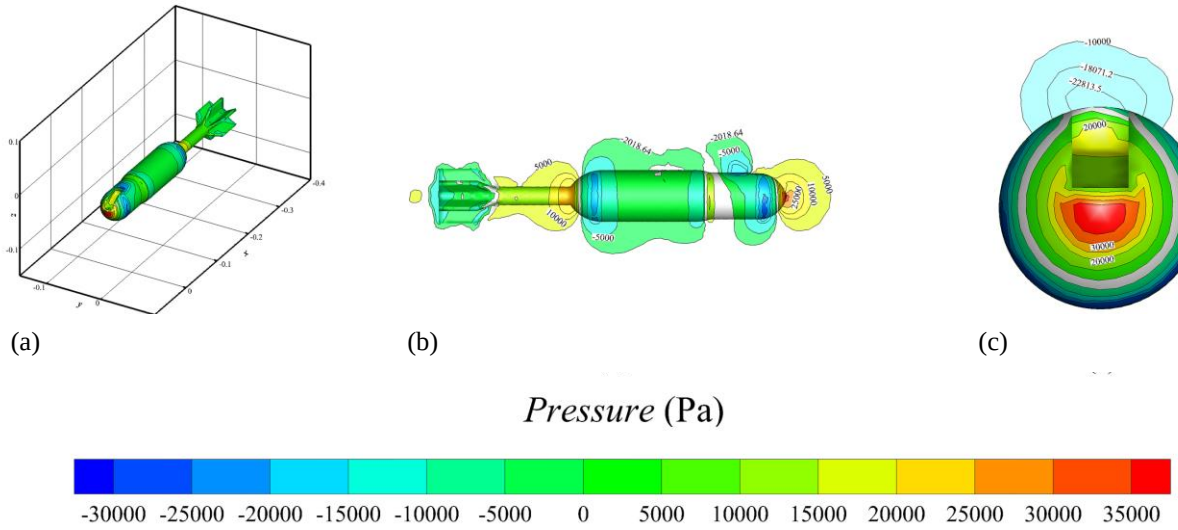

Fig. 11 Pressure distribution on surface and flow field of asymmetric nose projectile model

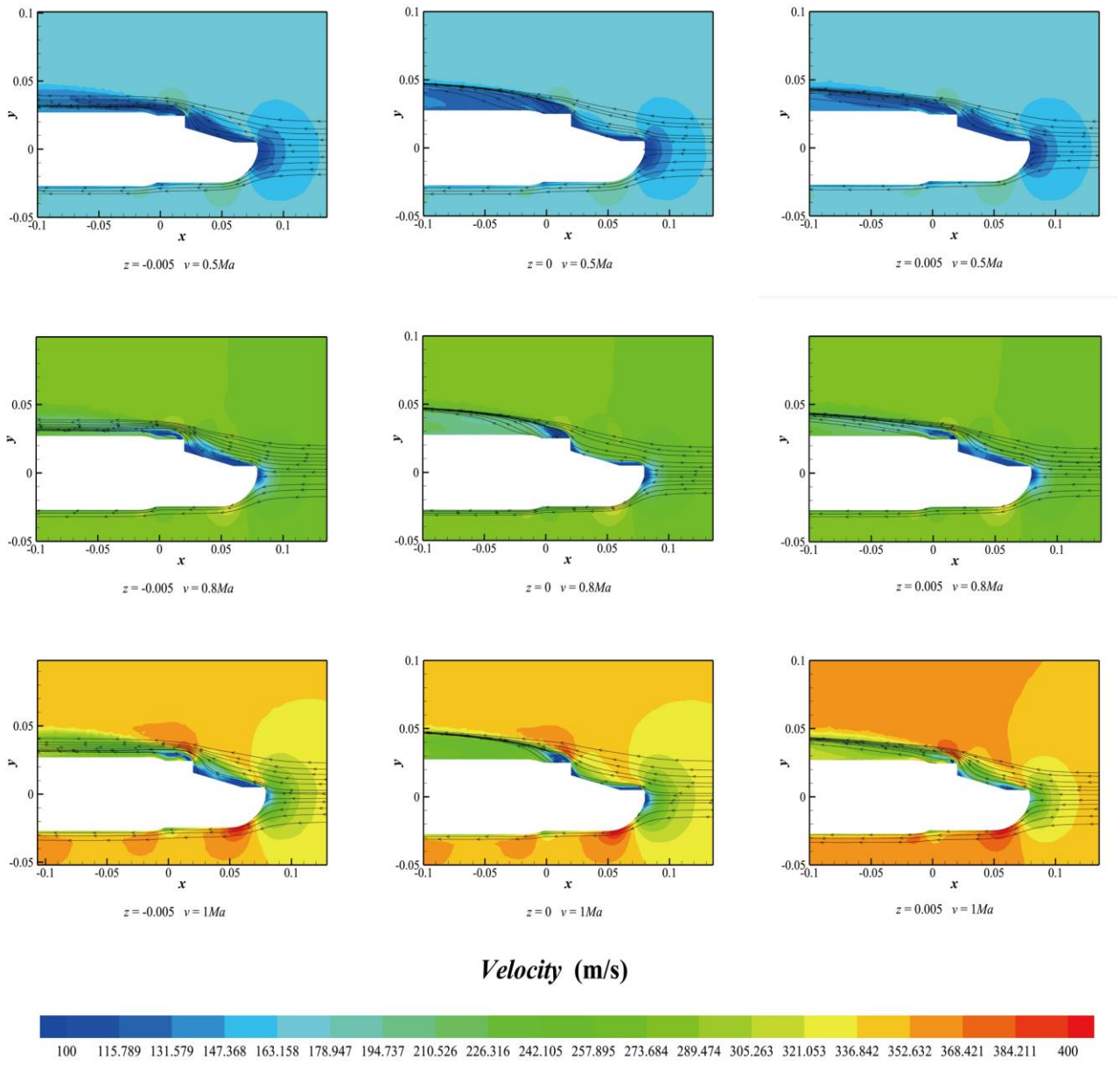

Fig. 14 Flow field distribution around diversion groove on surface of projectile nose

An analysis of Figs.11 and 12 reveals that the pressure produced by the structure of the diversion groove is considerably asymmetric on the upside and downside parts of the projectile. It can be observed from the figures that the velocity on the groove boundary layer is lower than that on the other side. The flow out of the groove still produces a low-velocity flow field on the upside parts of the projectile.

Figure 14 presents the velocity and streamline distributions at different sections inside the diversion groove at various Mach numbers. The airflow velocity of the fluted boundary layer is lower than that of the blunt nose of the projectile on the other side. After the fluid flows out of the groove, vortices are captured near the wall of the groove section, accompanied by the fluid separation phenomenon. The generation and intensity variation of asymmetric eddies are closely related to the groove parameters.

Quantitative Analysis of Asymmetric Flow Field

Analyzing the influence of the asymmetric nose on the asymmetric load requires a quantitative analysis of the projectile body's force. Using the established coordinate system, we examine the aerodynamic characteristics of the projectile through a theoretical analysis and model calculation, as illustrated in Fig.15. The forces that cause a ballistic deflection of the projectile mainly include gravity F_G, resistance F_N against the projectile's flight direction, and the aerodynamic force F_C on the inner surface of the groove. The deflection moment M_C is mainly concentrated in the head. Therefore, the force equation for the projectile can be represented as follows:

$$F_{Nx} + F_{Cx} + F_{Gx} = m\left(\frac{\mathrm{d}u}{\mathrm{d}t} + \omega v\right) \tag{8}$$

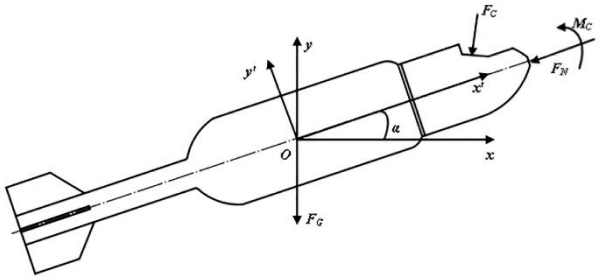

Fig. 15 Projectile stress analysis diagram

$$F_{Ny} + F_{Cy} + F_{Gy} = m\left(\frac{\mathrm{d}v}{\mathrm{d}t} - \omega u\right) \tag{9}$$

$$M_C = I_{zz}\frac{\mathrm{d}\omega}{\mathrm{d}t} \tag{10}$$

where F_{Nx}, F_{Cx} and F_{Gx} denote the force components in the x-axis direction; F_{Ny}, F_{Cy} and F_{Gy} represent the components of each force on the y-axis of the fixed coordinate system; u represents the velocity component in the x-axis direction; v represents the velocity component in the y-axis direction; ω represents the angular velocity around the pitch axis; and I_{yy} is the projectile inertia moment.

To compute the forces and moments acting on the projectile, the relationship between the fixed coordinate system and the projectile axis coordinate system is initially established. To convert the data from the elastic coordinate system to the fixed coordinate, the following intermediate transfer matrix can be used:

$$T_0 = \begin{bmatrix} \cos\alpha & -\sin\alpha \\ \sin\alpha & \cos\alpha \end{bmatrix} \tag{11}$$

Similarly, the intermediate transfer matrix from the fixed coordinate system to the elastic axis coordinate system can be written as:

$$T_p = \begin{bmatrix} \cos\alpha & \sin\alpha \\ -\sin\alpha & \cos\alpha \end{bmatrix} \tag{12}$$

Therefore, the transformation of the projectile gravity F_G to the projectile axis coordinate system can be expressed as:

$$\begin{bmatrix} F_{Gx} \\ F_{Gy} \end{bmatrix} = T_p \begin{bmatrix} 0 \\ mg \end{bmatrix} \tag{13}$$

The resistance F_N and aerodynamic F_C, forces can be expressed as:

$$F_N = \int_{S_N} P_N \boldsymbol{n}_N \mathrm{d}S_N \tag{14}$$

$$F_C = \int_{S_C} P_C \boldsymbol{n}_C \mathrm{d}S_C \tag{15}$$

where P_N denotes the surface pressure exerted on the blunt body at the nose of the projectile, P_C is the pressure on the surface of the groove, $\boldsymbol{n}_N$ is the external vector normal to the surface of the blunt body at the head, and $\boldsymbol{n}_C$ is the external vector normal to the surface of the groove. According to the theoretical model, the deflection aerodynamic force is closely related to the geometric surface area of the diversion groove.

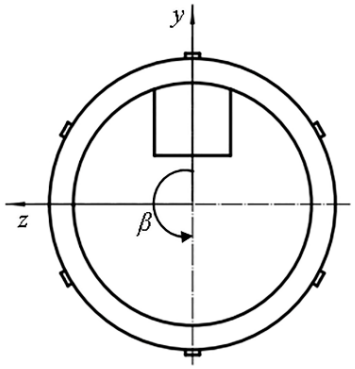

(a) Position angle of diversion groove β change

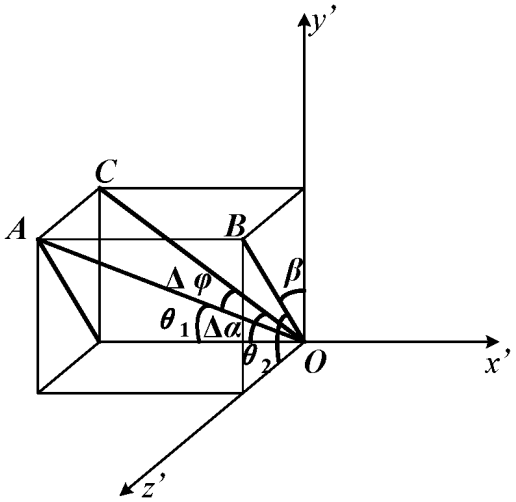

(b) Definition of additional angle of attack $\Delta\alpha$ and additional sideslip angle $\Delta\varphi$

Fig. 16 Decomposition diagram of the deflection angle of the diversion groove in the coordinate system

The initial position of the groove on the surface of the projectile nose is shown in Fig. 16(a). The central axis of the projectile coincides with the x-axis, and the symmetrical axis of the groove coincides with the y-axis. The right rotation of the groove position on the surface is completely symmetric to the left rotation, and the data of the groove rotation to the right can be converted from the experimental data of the left rotation. The lift force and drag obtained by the groove rotating to the right are the same as those of the left rotation; however, the yaw force coefficient and yaw moment have the same magnitude but opposite directions. We assume that the projectile is non-spinning and neglect the effects of the projectile tail on generating lift and rolling moment.

The angle definition in the projectile shaft coordinate system $Ox'y'z'$ is illustrated in Fig. 16(b). OA indicates the central axis of the inclined plane of the diversion groove.

OB is the projection of *OA* onto the *y'oz'* plane. The angle Δα between *OC* and the *x'*-axis is the additional angle of attack introduced by the groove. Positive values are defined for the angle above the *x'*-axis. The angle between *OA* and the *x'oy'* plane is defined as the additional sideslip angle $\Delta\varphi$. The angle defined to the right of *OA* is negative. The expressions of additional attack angle $\Delta\alpha$ and additional sideslip angle $\Delta\varphi$ obtained by coordinate transformation are as follows:

$$\Delta\alpha = -\arctan\left(\tan\theta\cos\beta\right) \tag{16}$$

$$\Delta\varphi = -\arctan\left(\sin\theta\sin\beta\right) \tag{17}$$

When the angle θ of the deflector is small, the Taylor series expansion is used to simplify Equations (16) and (17) as follows:

$$\Delta\alpha = -\theta\cos\beta \tag{18}$$

$$\Delta\varphi = -\theta\sin\beta \tag{19}$$

These expressions obtained for the aerodynamic coefficients of the asymmetric projectile are based on the analysis results of the aerodynamic characteristics of conventional projectiles. The projectile drag coefficient is expressed as:

$$c_x = c_{x0} + c_{cl} = c_{x0} + B\left(c_y + 0.5c_{x0}\right)^2 \tag{20}$$

where *B* is the induced drag factor, which is typically constant in transonic and subsonic states.

The projectile lift coefficient is expressed as:

$$c_y = c_{y0} + c_y^{\alpha}\alpha + c_y^{\Delta\alpha}\Delta\alpha \tag{21}$$

The projectile yaw coefficient is expressed as:

$$c_z = c_{z0} + c_z^{\varphi}\varphi + c_z^{\Delta\varphi}\Delta\varphi \tag{22}$$

where φ is the sideslip angle.

The projectile rolling moment coefficient is expressed as:

$$c_{mx} = c_{mx0} + c_{mx}^{\varphi}\varphi + c_{mx}^{\Delta\varphi}\Delta\varphi + c_{mx}^{\omega_x}\omega_x + c_{mx}^{\omega_y}\omega_y \tag{23}$$

where ω_x is the angular velocity of rotation about the *x*-axis, and ω_y is the angular velocity of rotation about the *y*-axis.

The projectile yaw moment coefficient is expressed as:

$$c_{my} = c_{my0} + c_{my}^{\varphi}\varphi + c_{my}^{\Delta\varphi}\Delta\varphi + c_{my}^{\omega_y}\omega_y + c_{my}^{\omega_x}\omega_x \tag{24}$$

The projectile pitching moment coefficient is expressed as:

$$c_{mz} = c_{mz0} + c_{mz}^{\alpha}\alpha + c_{mz}^{\Delta\alpha} + c_{mz}^{\omega_z}\omega_z \tag{25}$$

where ω_z is the angular velocity of rotation about the *z*-axis.

Assuming the downward effect of the diversion groove on the tail is disregarded during the flight of the projectile, then:

$$\varphi = 0^{\circ}, \omega_x = \omega_y = \omega_z = 0\text{rad/s} \tag{26}$$

Therefore, the aerodynamic coefficient of the projectile is finally simplified to:

$$\begin{cases} c_x = c_{x0} + B\left(c_y + 0.5c_{x0}\right)^2 \\ c_y = c_{y0} + c_y^{\alpha}\alpha - c_y^{\Delta\alpha}\theta\cos\beta \\ c_z = c_{z0} - c_y^{\Delta\varphi}\theta\sin\beta \\ c_{mx} = 0 \\ c_{my} = c_{my0} - c_{my}^{\Delta\varphi}\theta\sin\beta \\ c_{mz} = c_{mz0} + c_{mz}^{\alpha}\alpha - c_{mz}^{\Delta\alpha}\theta\cos\beta \end{cases} \tag{27}$$

According to the aerodynamics theory, when the projectile flies within the small angle of attack, then:

$$\begin{cases} c_y^{\alpha} = \dfrac{\mathrm{d}c_y}{\mathrm{d}\alpha} = const1 \\ c_{mz}^{\alpha} = \dfrac{\mathrm{d}c_{mz}}{\mathrm{d}\alpha} = const2 \end{cases} \tag{28}$$

Therefore, c_y, c_z, c_{my} and c_{mz} can be modified by changing the structural parameters θ and position angle β of the diversion groove.

5. ANALYSIS OF MAIN INFLUENCING FACTORS

The main factors influencing the aerodynamic characteristics of a projectile include its geometric shape, surface details, material properties, angle of attack, velocity, and rotation. The geometric shape and surface details of a projectile affect the distribution of aerodynamic forces and the generation of drag. The angle of attack and velocity alter the flow pattern, influencing the generation of lift, drag, and side force. The rotation of a projectile alters the distribution of aerodynamic forces, affecting the stability and trajectory of the projectile. Owing to the relatively small rotation speed angle of the tail-stabilized projectile, based on the research conducted by Liang et al. (2017) on the optimization design of projectile structures, we examined the effects of diversion groove structures on the aerodynamic characteristics of the projectile in terms of velocity and angle of attack.

5.1 Effect of Velocity on Aerodynamic Characteristics

The aerodynamic simulation analysis of the asymmetric nose projectile model was performed in the established coordinate system and in the outflow field. Speeds of 0.5 Ma, 0.8 Ma, and 1 Ma were set in the simulation according to the actual flight process of the mortar. Selecting these speeds essentially covers key velocity values during the projectile's trajectory flight. The corresponding Reynolds numbers were 6.98×10^5, 1.17×10^6, and 1.4×10^6, respectively. To examine the effect of different diversion groove positions on aerodynamic performance, we changed angle β from 0° to 180° in the counterclockwise direction during the simulation (one groove working position is obtained every 10°). Numerical computations were conducted for each working

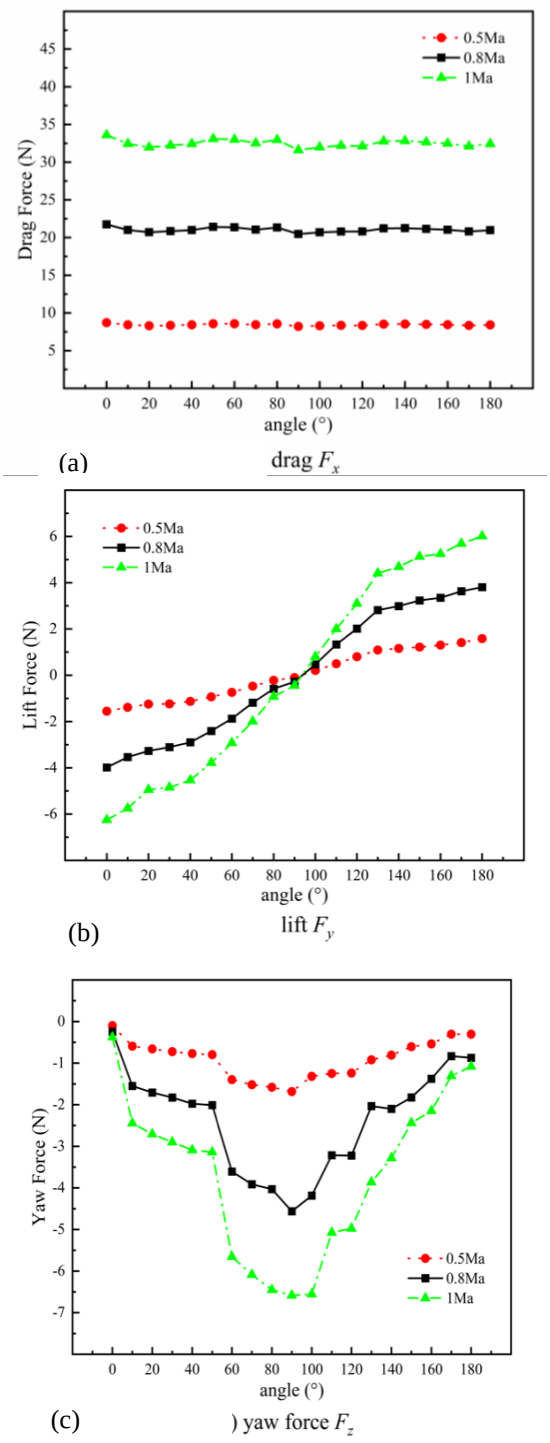

Fig. 17 Variation trends of (a) drag F_x (b) lift F_y and (c) yaw force F_z, each with β at different speeds

position of the projectile, yielding aerodynamic characteristic data under different velocity conditions. Then, the data was organized and analyzed to summarize the patterns of aerodynamic characteristic variations.

5.1.1 Relationship Between Velocity and Aerodynamic Force

Figure 17 illustrates the variation trends of the drag force, lift force, and yaw force of the projectile and the position angle of the grooves on the surface at different speeds. Figure 17(a) shows that the projectile resistance increases with increasing velocity, and no clear relationship is observed between the groove angle and resistance. Figure 17(b) illustrates the change in lift force. From β = 0° to β = 90°, the lift force in the -y direction gradually decreases until the central axis of the groove reconnects with the z-axis. From β = 90° to β = 180°, the lift gradually increases in the +y direction. Figure 17(c) presents the change between the groove position angle β and yaw force at different flow rates. When β deviates counterclockwise from the initial position, the projectile generates a yaw force in the -z direction. The maximum yaw force is generated between β = 90° and β = 100°. For values of β greater than 100°, the yaw force shows an obvious decreasing trend until β = 180°, after which the yaw force disappears.

5.1.2 Relationship Between Velocity and Force Coefficient

Equations (5)−(7) are also used to make the aerodynamic force dimensionless, and the variation trends of drag coefficient C_x, lift coefficient C_y, and yaw force coefficient C_z are obtained, as illustrated in Fig. 18. Based on the data depicted in Fig. 18, the aerodynamic component coefficients of the same groove position angle β are close under different velocity conditions. This implies that the change in projectile velocity does not affect the aerodynamic coefficients, thus eliminating the interference of velocity factors. Hence, understanding the variation trend between the aerodynamic coefficient and groove position angle β has a significant reference value for analyzing the aerodynamic characteristics of projectiles.

5.1.3 Relationship Between Velocity and Moment Coefficient

The simulation results provide the aerodynamic torque of the projectile. Equations (29)−(31) are used to perform the dimensionless processing, and the variation of the projectile rolling moment coefficient C_{mx}, yaw moment coefficient C_{my}, and pitching moment coefficient C_{mz} with groove position angle β is obtained, as illustrated in Fig. 19.

$$C_{mx} = \frac{M_x}{0.5\times\rho\times V^2\times S\times l} \tag{29}$$

$$C_{my} = \frac{M_y}{0.5\times\rho\times V^2\times S\times l} \tag{30}$$

$$C_{mz} = \frac{M_z}{0.5\times\rho\times V^2\times S\times l} \tag{31}$$

where M_x is the rolling moment, M_y is the projectile yaw moment, M_z is the pitching moment, V is the fluid velocity, ρ is air density, and S is the characteristic area, that is, the maximum cross-sectional area of the projectile.

As observed from Fig. 19(a), for a 0° angle of attack, the coefficient of rolling moment of the projectile about the x-axis fluctuates between -0.002 and 0.004. Hence, we get C_{mx} = 0. Figure 19(b) illustrates the yaw moment coefficient C_{my} of the projectile's lateral deflection around the y-axis. Figure 19(c) shows the change in the pitch moment coefficient of a projectile around the z-axis.

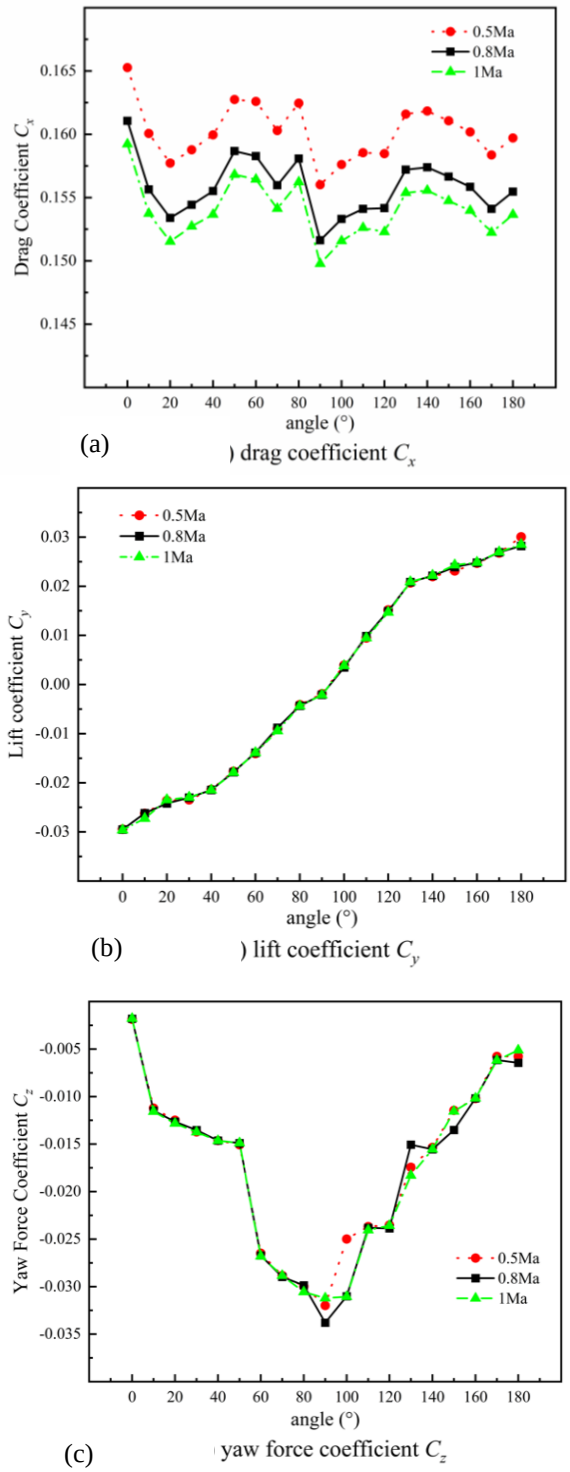

Fig. 18 Variation trends of (a) drag coefficient C_x (b) lift coefficient C_y, and (c) yaw force coefficient C_z, each with β at different speeds

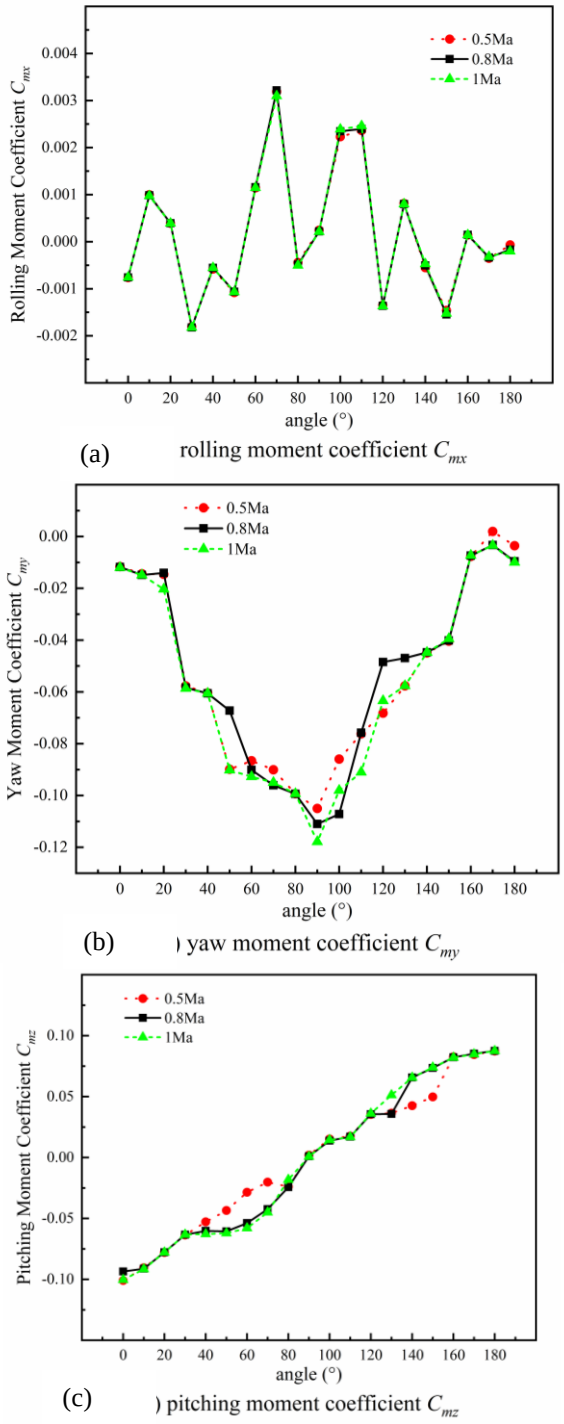

Fig. 19 Variation trend of (a) rolling moment coefficient C_{mx}, (b) yaw moment coefficient C_{my}, and (c) pitching moment coefficient C_{mz}, each with β at different speeds

5.2 Effect of Angle of Attack on Aerodynamic Characteristics

The angle of attack also affects the aerodynamic coefficient. Therefore, it is imperative to comprehensively investigate the aerodynamic characteristics resulting from the combined effects of the diversion groove and the angle of attack.

Considering a velocity of 0.8 Ma, the aerodynamic characteristics of four projectile attitudes with an angle of attack α of -6°, -3°, 3°, and 6° are compared with those of a projectile attitude with 0° angle of attack. ±3° simulates changes in aerodynamic characteristics under small pitch angle variations of the projectile, while ±6° simulates changes in aerodynamic characteristics under large pitch angle variations. Aerodynamic characteristic data was obtained at each projectile's working position under different angles of attack attitudes. Then, the data was organized to identify the patterns of their variations.

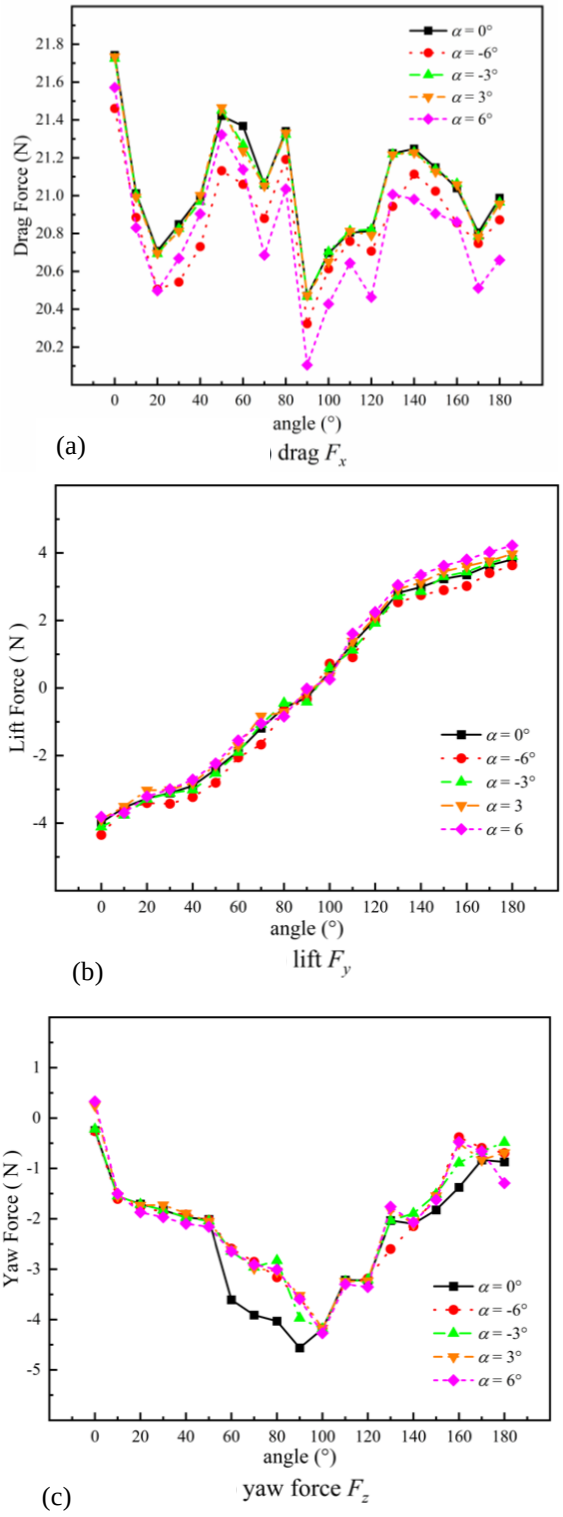

Fig. 20 Variation trend of (a) drag F_x, (b) lift F_y, and (c) yaw force F_z, each with β at different angles of attack

5.2.1 Relationship Between Angles of Attack and Aerodynamic Force and Coefficient

In Figs. 20(a) and 21(a), the attacking angles have no significant effect on the resistance. Figures 20(b) and 21(b) present the variation trend of the projectile lift. When the projectile head angle of attack deflects downward, the projectile body generates a downward negative lift force; hence, the lift force in the -*y* direction generated by β between 0° and 90° is larger than that of other angles of attack. Similarly, when the projectile head angle of attack deflects upward, the projectile body generates an upward positive lift; hence, the +*y* lift generated by β between 90° and 180° is greater than that of other angles of attack. Figures 20(c) and 21(c) illustrate the variation trend of the yaw force under different attitude angles of attack. According to the yaw force distribution shown in the figure, when the groove angle is between 60° and 100°, the yaw force in the -*y* direction induced by the groove at an inclined attitude is relatively lower compared to the condition without an angle of attack. The maximum yaw force is obtained when β = 100°.

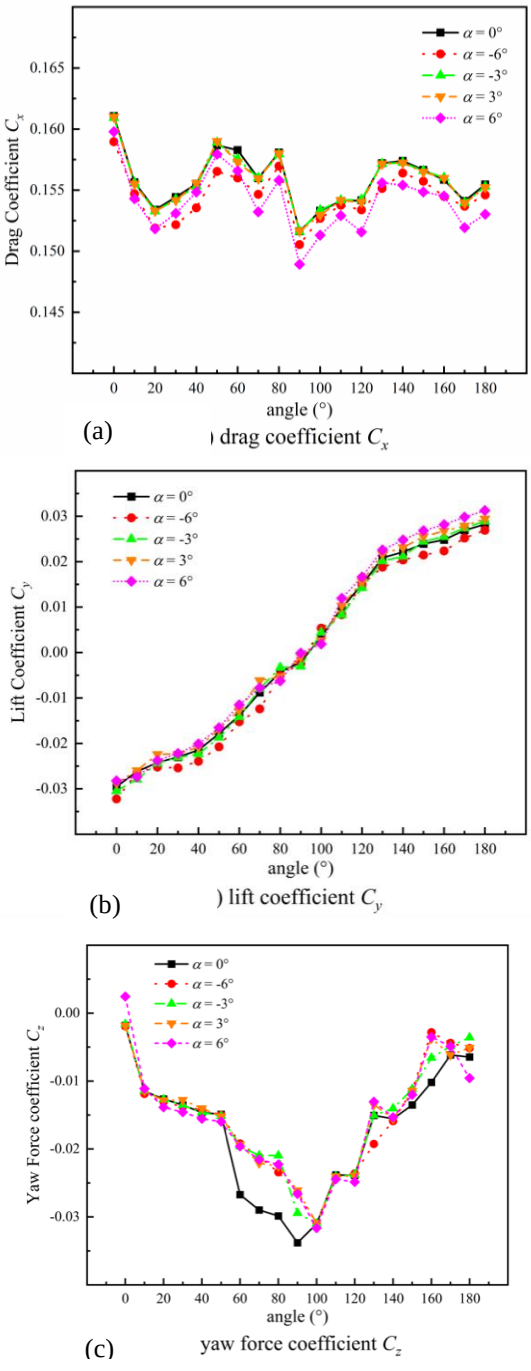

Fig. 21 Variation trend of (a) drag coefficient C_x, (b) lift coefficient C_y, and (c) yaw force coefficient C_z, each with β at different angles of attack

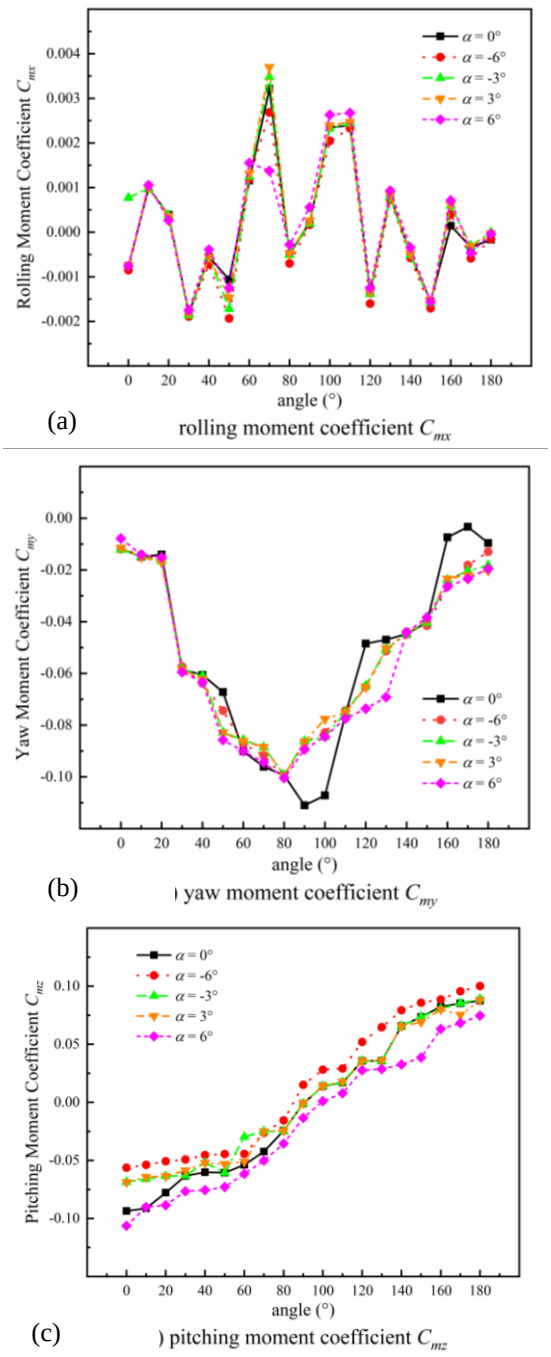

Fig. 22 Variation trend of (a) rolling moment coefficient C_{mx}, (b) yaw moment coefficient C_{my}, and (c) pitching moment coefficient C_{mz}, each with β at different angles of attack

5.2.2 Relationship Between Angles of Attack and Moment Coefficient

Figure 22 depicts the changes in aerodynamic torque coefficients as the groove position angle β varies under different angles of attack. From Fig. 22(a), it can be concluded that the rolling moment coefficient remains relatively consistent across various angles of attack. Figure 22(b) shows that when $\alpha \neq 0°$, the maximum yaw moment coefficient generated when the angle lies between 80° and 100° is lower than that generated at a 0° angle of attack. Figure 22(c) presents the pitch moment factor around the z-axis. Comparing the variation trend of the projectile at an angle of attack of 0°, we observe that the pitching moment generated by the aerodynamic force exhibits a similar trend with β for the projectile angles of attack of 3° and -3°. When α = 6°, the groove angle lies between 0° and 80°, and the projectile generates a larger downward pitching moment. When the groove angle is 100°−180°, the upward pitching moment generated by the projectile decreases. When α = -6° and the angle of the groove is 0°−80°, the moment generated by the head of the projectile is less than that of the 0° angle of attack, and the moment generated by the groove angle of 100°−180° is greater than that of the 0° angle of attack attitude.

6. QUALITATIVE RESULTS OF PROJECTILE AERODYNAMIC PERFORMANCE

The analysis of simulation data reveals that there is a relationship between the deflection angle of the diversion groove and the aerodynamic characteristics under different velocities and angles of attacks. Accurately summarizing these patterns of change is significant for the subsequent research on the optimization of the tail-stabilized projectile structure with asymmetrical diversion groove and ballistic correction control. By summarizing the data analysis results in Section 5, the following conclusions are Obtained.

6.1 Variations in Aerodynamic Characteristics with Different Velocities

Aerodynamic forces are closely related to velocity. The Fig. 17 clearly demonstrate a progressive rise in the aerodynamic forces exerted on the projectile as the flow velocity increases. The aerodynamic forces acting on the projectile are directly proportional to the flow velocity. The variation in the deflection angle of the diversion groove primarily affects the direction of the lift and yaw forces acting on the projectile.

Aerodynamic coefficients can be utilized to establish a relationship between the phase angle of the diversion groove and the projectile's aerodynamic characteristics. Figure 18 indicates that velocity does not considerably affect the aerodynamic force coefficients. The drag coefficient C_x fluctuates within a small range; the lift coefficient C_y changes with angle β and approximates a cosine function; and the yaw coefficient C_z changes with angle β and approximates a sine distribution.

The projectile's aerodynamic moment coefficient is also related to the groove's phase angle. As shown in Fig. 19, the diversion groove does not considerably influence the rolling behavior. The yaw moment coefficient exhibits an approximate sinusoidal trend with respect to the angle β. The pitching moment coefficient C_{mz} exhibits an approximately cosine trend with respect to the angle β.

6.2 Variations in Aerodynamic Characteristics with Different Angles of Attack

The presence of an angle of attack induces changes in the projectile's flight attitude, leading to variations in the contact area between the deflector and the airflow. Small variations in the angle of attack do not cause considerable

fluctuations in aerodynamic drag; however, small variations have an impact on the lift and yaw forces experienced by the projectile. The trend of lift change is positively correlated with the variation of the angle of attack. The angle of attack causes the maximum yawing force to occur at $\beta = 100°$, which is because of the change in contact area between the diversion trough and the air flow in the presence of the angle of attack.

The analysis of the principle, indicates that when $\alpha > 0°$, the projectile body generates an upward positive lift, and the aerodynamic center is positioned behind the projectile's center of mass (calculated from the warhead). Thus, because of the angle of attack, the projectile produces a moment with its head deflecting downward. When the diversion groove induces negative lift at the head of the projectile, the downward pitching moment of the projectile increase. When the groove generates positive lift, the negative lift generated by the angle of attack partially offsets the positive lift, decreasing the upward pitching moment of the projectile. Similarly, when $\alpha < 0°$, the downward moment generated by the groove decreases, and the upward moment increases.

7. QUANTITATIVE RESULTS OF PROJECTILE AERODYNAMIC PERFORMANCE

The flight performance of the projectile is closely related to the stability and maneuverability of the projectile body. The projectile's structure must have sufficient stability and corrective capability while minimizing aerodynamic drag. This paper evaluated the projectile's stability and maneuverability from three aspects: aerodynamic drag and corrective force, static margin, and differences between simulation data and mathematical expressions. By performing a quantitative analysis in these three aspects, this paper draws the following conclusions.

7.1 Aerodynamic Drag and Corrective Force

An appropriate projectile structure design should minimize the aerodynamic drag of the projectile. For unpowered tail-stabilized projectiles, lower aerodynamic drag translates to reduced energy loss and increased range. Thus, aerodynamic drag is often considered the primary criterion for evaluating the aerodynamic design of projectiles. The corrective mechanism needs to convert aerodynamic forces into corrective forces more effectively, thereby enhancing the correction efficiency.

The aerodynamic characteristics simulated in this study are compared with the wind tunnel experimental data of a conventional tail-stabilized projectile and a canard-controlled projectile. The conditions for the data in Fig. 23 are 0.5 Ma, and a 0° angle of attack.

An analysis of the data shows that the asymmetric diversion groove design reduces the drag coefficient of the projectile by 4.1%, which is 1.2% lower than the drag reduction achieved by the canard rudder control mechanism in conventional projectiles. The lift coefficient and pitch moment coefficient of the asymmetric diversion groove design increased by 6.4% and 16%, respectively, compared to those of the canard rudder control mechanism.

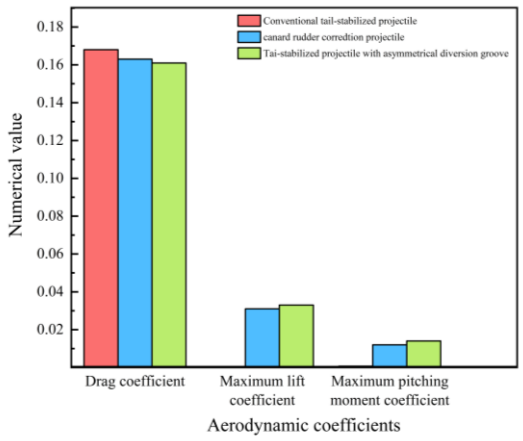

Fig. 23 Comparison of aerodynamic coefficient data

The comparison of the data reveals that under subsonic conditions, the tail-stabilized projectile with an asymmetrical diversion groove can reduce the aerodynamic drag compared to the commonly used canard rudder correction mechanism. This is advantageous for increasing the projectile's range. Meanwhile, an appropriate groove's phase angle leads to a higher maximum corrective force coefficient for the projectile compared to the commonly used canard-control mechanism. Therefore, the diversion groove structure demonstrates good corrective capabilities for the projectile within the subsonic range.

7.2 static Margin

The projectile needs to maintain adequate stability during its flight while ensuring that it can undergo flight attitude changes due to the action of the corrective mechanism. All of these factors are related to the overall stability and maneuverability of the projectile. The static margin is commonly used to evaluate the rationality of the overall projectile structural design.

The static margin is used to assess the flight stability of the projectile in a static equilibrium state. In the flight process, the center of pressure of the projectile is located at the center of mass, and it is related to the projectile's velocity and angle of attack. The further the center of pressure is from the center of mass, the greater the torque required to change the flight attitude, and the higher the stability. However, an excessively high static margin makes it more difficult to adjust the projectile's flight attitude. Therefore, to improve the correction capability of the projectile, a too-large static margin is undesirable. However, a too-small static margin indicates poor stability of the projectile during flight. Therefore, during the projectile's flight, its static margin should be maintained within a reasonable range. The expression for static margin is as follows:

$$\eta = \frac{\Delta x}{l} \times 100\% = \frac{x_p(t) - x_c(t)}{l} \times 100\% \tag{32}$$

where $x_p(t)$ represents the position of the projectile's center of pressure, and $x_c(t)$ represents the position of the projectile's center of mass, and both vary with changes in the flight attitude during the flight process.

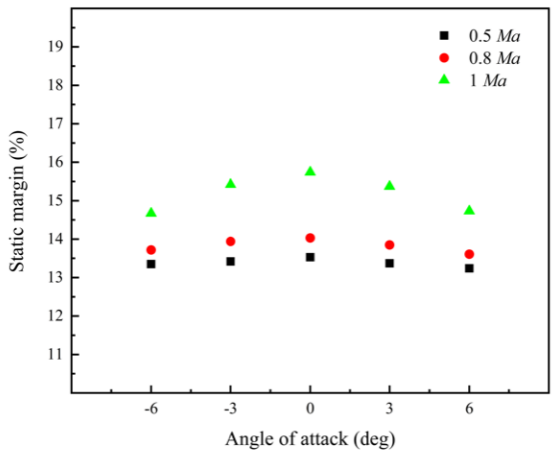

Fig. 24 Static margins of model with diversion groove at different angles of attack and Mach numbers

For nose-stabilized projectile correction structures, the typical range for the static margin is between 10% and 25%. Figure 24 shows the static margin of the head-stabilized non-symmetric diversion groove projectile at different Mach numbers and angles of attack. From the data, it can be observed that the static stability margin of the tail-stabilized projectile with asymmetrical diversion groove is in the range of 13% to 16%. This result indicates that the overall structural correction capability of the projectile is moderate, and the stability is good.

7.3 Analysis of Discrepancy Between Simulation Data and Mathematical Expressions

In § 4.3, Expression (27) for the projectile's aerodynamic coefficients is derived through theoretical analysis. This expression establishes the functional relationship between C_y, C_z, C_{my}, and C_{mz} with the deflection angle β of the diversion groove. In Section 5, aerodynamic characteristic data generated at different diversion groove working positions were obtained through numerical simulations, followed by data processing and analysis. In Section 6, based on the simulation data, the variation patterns of aerodynamic coefficients with the diversion groove phase angle β are summarized. Then, the reliability of the conclusions drawn from simulation data is validated by analyzing the errors between simulation results and mathematical expressions.

Based on Expression (27) and the simulation data, the following two conclusions can be drawn. Firstly, the aerodynamic drag of the projectile shows no significant variation, and the roll torque is zero. Meanwhile, changes in the angle of attack do not fundamentally change the variation pattern of aerodynamic coefficients. Thus, the validation work did not focus on aerodynamic drag and was conducted under the condition of α = 0°. By investigating the aerodynamic characteristics of the conventional blunt-nose projectile in § 4.1, the numerical values of the parameters c_{y0}, c_{z0}, c_{my0}, and c_{mz0} in Expression (27) can be obtained. The projectile model's θ = 10°. By substituting the parameter values into Expression (27), we have:

$$\begin{cases} C_y = 0.008 - 0.0271\cos\beta \\ C_z = -0.007 - 0.0371\sin\beta \\ C_{my} = 0.007 - 0.0812\sin\beta \\ C_{mz} = -0.006 - 0.0853\cos\beta \end{cases} \tag{33}$$

Fitting the simulated data according to the form of Expression (27), the fitting function is obtained:

$$\begin{cases} C_y = 0.0002 - 0.0269\cos\beta \\ C_z = -0.0025 - 0.0249\sin\beta \\ C_{my} = 0.005 - 0.0965\sin\beta \\ C_{mz} = -0.003775 - 0.0905\cos\beta \end{cases} \tag{34}$$

Figure 25 provides a comparative analysis between the theoretical curve, fitting curve, and simulated data. From this figure, it can be seen that the variation trend of the simulated aerodynamic coefficients aligns closely with the mathematical expression. This study employed the Sum of Squares due to Error (SSE) and Root Mean Squared Error (RMSE) as metrics to evaluate the errors between the simulated data and the theoretical expression as well as the fitted function. Smaller values of SSE and RMSE indicate better predictive accuracy and higher precision of the model.

The sum of squares due to the error and root mean squared error of the aerodynamic coefficients are shown in Fig. 26. The figure shows that the sum of squares due to the error between the simulated data and the mathematical expression are 3.486×10^{-5}, 6.519×10^{-4}, 4.7×10^{-3}, and 1.1×10^{-3}, respectively. The root mean squared errors are 0.0014, 0.006, 0.0162, and 0.0078, respectively. The sum of squares due to errors between the simulated data and the fitting function are 2.8032×10^{-5}, 2.4186×10^{-4}, 4.1×10^{-3}, and 9.88×10^{-4}, respectively. The root mean squared errors are 0.0013, 0.0038, 0.0155, and 0.0076, respectively. Based on this, it can be inferred that the simulation data are generally distributed around the theoretical curve. Also, the deviation between the theoretical curve and the data fitting curve is relatively small.

8. CONCLUSIONS

In this paper, a ballistic correction theory for an asymmetric nose projectile model is proposed by referring to previous research on the aerodynamic characteristics of the diversion groove. Qualitative and quantitative analyses are performed on a simplified asymmetric nose projectile model, and numerical simulations are conducted under different Mach numbers and angles of attack. The principal findings of this study are as follows:

(1) Numerical analysis was conducted on conventional and asymmetrical projectiles under defined external flow field conditions. The results showed that the conventional blunt-nose projectile model maintains a symmetric flow field distribution. However, incorporating a diversion groove structure at the projectile nose induces asymmetry in the flow field surrounding the projectile, thereby generating yaw force and moment.

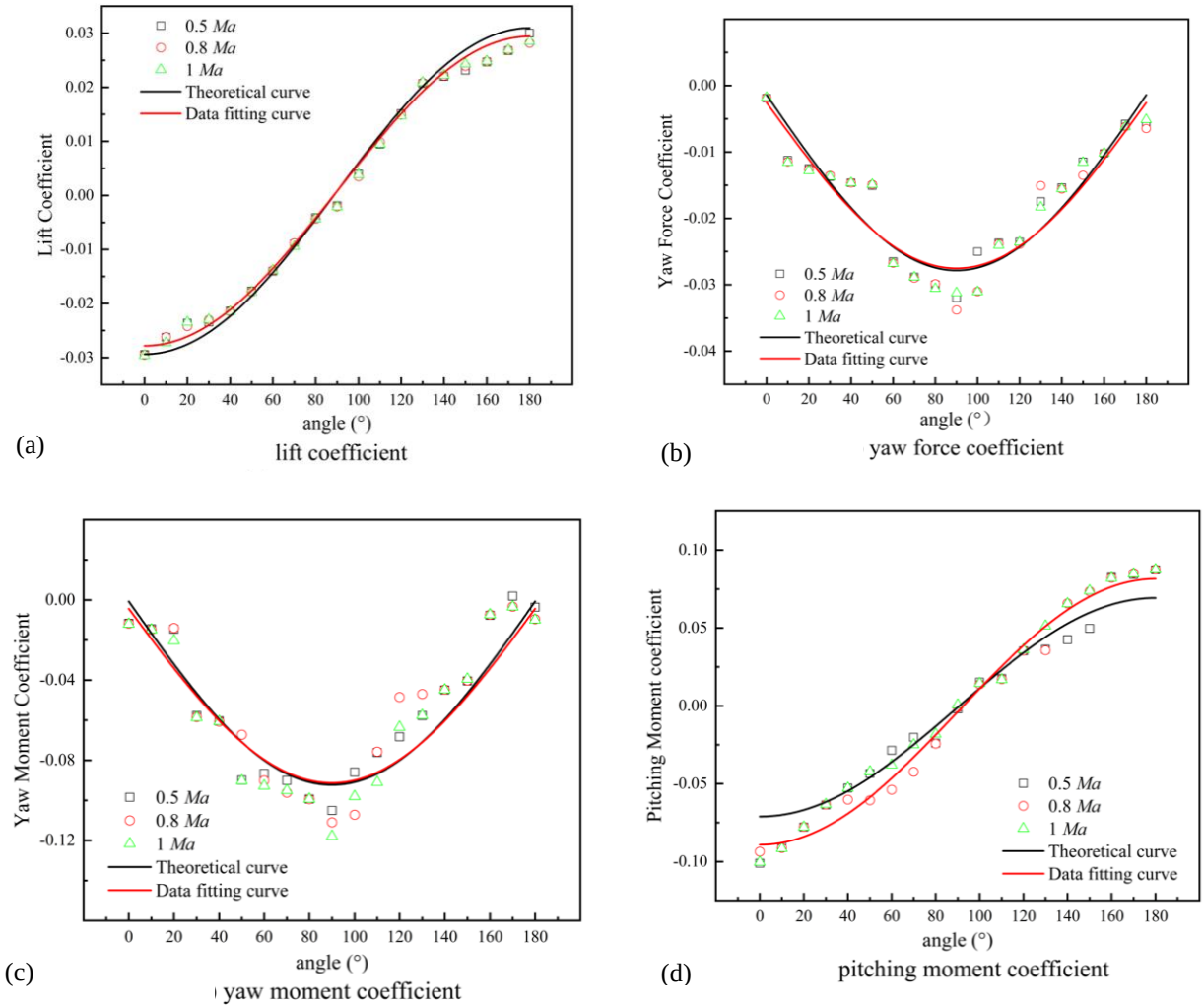

Fig. 25 Comparison of theoretical and fitting curves of aerodynamic coefficients with simulated data

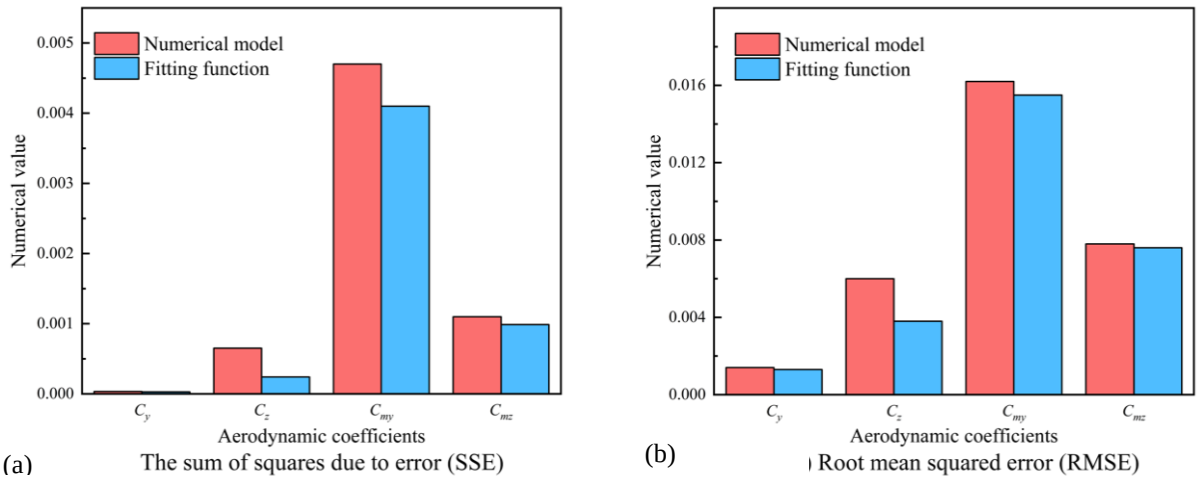

Fig. 26 Error analysis of theoretical expression and fitting function

(2) By observing the flow state of the airflow near the diversion groove under different Mach numbers, we observed that fluid separation and vortex generation occurred after the flow passes through the diversion trough. The increase in Mach number causes an increase in the aerodynamic force acting on the projectile. Meanwhile, we derived the mathematical expressions for the projectile aerodynamic coefficient with respect to the angle of attack α and the deflection angle β of the diversion groove.

(3) A numerical simulation of the asymmetric nose projectile model was performed. The variation of the aerodynamic coefficient with the deflection angle of the diversion groove trough under different Mach numbers was studied. The study showed that the variation trends of the lift coefficient and pitching moment coefficient with

respect to the angle β approximate a cosine function, while the variation trends of the yaw force coefficient and yaw moment coefficient with respect to the angle β approximate a sine function. The simulation results and predictions of aerodynamic forces and moments from the static mathematical model are in good agreement with respect to the variation of the deflection angle of the diversion groove. Additionally, we analyzed the variation patterns of the projectile's aerodynamic coefficients under different angles of attack and found that when the angle of attack α exceeds ±6°, the aerodynamic characteristics of the projectile intensify with increasing angle of attack.

(4) We compared the simulation results under the conditions of 0.5 Ma and 0° angle of attack and the experimental data of a certain model of conventional tail-stabilized projectile and duck-bill control projectile in terms of their aerodynamic characteristics. The tail-stabilized projectile with asymmetrical diversion groove exhibited a 1.2% decrease in drag coefficient compared to that of the duck-bill control projectile. Furthermore, the non-symmetric flow-control groove tail-stabilized projectile showed an increase of 6.4% in lift coefficient and 16% in pitching moment coefficient. Furthermore, the static stability margin of the non-symmetric flow-control groove tail-stabilized projectile falls within the range of 13% to 16%. This phenomenon indicates that the overall structure of the tail-stabilized projectile with asymmetrical diversion grooves exhibits good correction capability and stability.

The findings of this study serve as a valuable reference for the design of corrective structures and trajectory control involving diversion grooves. The findings contribute to the understanding of the aerodynamic behavior of projectiles and offer insights into optimizing their performance. However, this study only focused on the numerical study of the non-rotating, displacement-stabilized projectile, and the aerodynamic attributes of the rotating projectile should be further improved in a future work.

ACKNOWLEDGEMENTS

This work is supported by the National Defense Pre-Research Foundation (Grant No. 61402060103). The authors would like to thank all the reviewers who participated in the review, as well as MJEditor (www.mjeditor.com) for providing English editing services during the preparation of this manuscript.

CONFLICT OF INTEREST

The authors declare that they have no known competing financial interests or personal relationships that could have appeared to influence the work reported in this paper.

AUTHORS CONTRIBUTION

Angang Luo: Methodology, Software, Writing – origina draft. **Qinkun Xiao:** Supervision, Writing – review. **Xing Liu:** Conceptualization, Writing – review & editing. **Jiachong Guo:** Visualization, Plotting engineering drawing. **Yinhuan Zhang:** Visualization, Plotting engineering drawing.

REFERENCES

Bernhardt, J. E. (2000). Closed-loop control of forebody flow asymmetry. *Journal of Aircraft*, *37*(3), 491-498 https://doi.org/10.2514/2.2624

Cui, S., Liu, X., Jiang, S., & Guo, J. (2022). Control strategies for flight stability of trajectory correction projectile with air-ducts structure. *Mathematical Problems in Engineering*. https://doi.org/10.1155/2022/1383294

Ericsson, L. E. (1993). Unsteady flow separation on slender bodies at high angles of attack. *Journal of Spacecraft and Rockets*, *30*(6): 689-695. https://doi.org/10.2514/3.26374

Ganesan, S., & Esakki, B. (2020). Computational fluid dynamic analysis of an unmanned amphibious aerial vehicle for drag reduction. *International Journal of Intelligent Unmanned Systems*, *8*(3), 187-200. https://www.emerald.com/insight/content/doi/10.1108/IJIUS-01-2019-0003/full/html

Goddard, R. H. (1952). *Apparatus for steering aircraft*. US.

Hamel, N., & Gagnon, E. (2011). *CFD and Parametric Study on a 155mm Artillery Shell Equipped with a Roll-Decoupled Course Correction Fuze*. 29th AIAA Applied Aerodynamics Conference. American Institute of Aeronautics and Astronautics. https://doi.org/10.2514/6.2011-3027

Hooker, R. D. (2005). *Beyond Vom Kriege: The character and conduct of modern war*. Parameters. https://doi.org/10.55540/0031-1723.2256

Landers, M., & Auman, L. (2001). *Experimental investigation of nose-mounted controls for a hypersonic missile.* 19th AIAA Applied Aerodynamics Conference. American Institute of Aeronautics and Astronautics. https://doi.org/10.2514/6.2001-2433

Landers, M., Hall, L., Auman, L., & Vaughn, M. (2003). *Deflectable nose and canard controls for a fin-stabilized projectile at supersonic and hypersonic speeds.* 21st AIAA Applied Aerodynamics Conference. American Institute of Aeronautics and Astronautics. https://doi.org/10.2514/6.2003-3805

Liang, K., Huang, Z., & Zhang, J. M. (2017). Optimal design of the aerodynamic parameters for a supersonic two-dimensional guided artillery projectile. *Defence Technology*, *13*(3), 206-211. http://dx.doi.org/10.1016/j.dt.2017.05.003

Lin, M., & Sarlak, H. (2016). *A comparative study on the flow over an airfoil using transitional turbulence models.* AIP Conference Series. AIP Publishing LLC. https://doi.org/10.1063/1.4951806

Liu, Y., Li, P. F., He, W., & Jiang, K. Y. (2020). Numerical study of the effect of surface grooves on the aerodynamic performance of a NACA 4415 airfoil for small wind turbines. *Journal of Wind Engineering and Industrial Aerodynamics*, *206*, 104263. https://doi.org/10.1016/j.jweia.2020.104263

Liu, Y., Li, P. F., & Jiang, K. Y. (2021). Comparative assessment of transitional turbulence models for airfoil aerodynamics in the low Reynolds number range. *Journal of Wind Engineering and Industrial Aerodynamics*, *217*, 104726. https://doi.org/10.1016/j.jweia.2021.104726

Mariotti, A., Buresti, G., Gaggini, G., & Salvetti, M. V. (2017). Separation control and drag reduction for boat-tailed axisymmetric bodies through contoured transverse grooves. *Journal of Fluid Mechanics*, *832*, 514-549. https://doi.org/10.1017/jfm.2017.676

Marshall, D. (2005). *High speed aerodynamics of novel missile configurations*. [MS Thesis, School of Engineering, Cranfield University].

Massey, K., & Flick, A. (2007). *Mechanical and Jet actuators for guiding a small caliber subsonic projectile*. 25th AIAA Applied Aerodynamics Conference. American Institute of Aeronautics and Astronautics. https://doi.org/10.2514/6.2007-3813

Massey, K., McMichael, J., Warnock, T., & Hay, F. (2008). Mechanical Actuators for Guidance of a Supersonic Projectile. *Journal of Spacecraft and Rockets*, *45*(4), 802-812. https://doi.org/10.2514/1.31709

May, A. (1952). Vertical entry of missiles into water. *Journal of Applied Physics*, *23*(12), 1362-1372. https://doi.org/10.1063/1.1702076

May, A. (1975). *Water entry and the cavity-running behavior of missiles*. Navsea Hydroballistics Advisory Committee, Silver Spring. https://apps.dtic.mil/sti/citations/ADA020429

Menter F. R. (2009). Review of the shear-stress transport turbulence model experience from an industrial perspective. *International Journal of Computational Fluid Dynamics*, *23*(4), 305-316. https://doi.org/10.1080/10618560902773387

Pan, Z. Y., Cui, W. C., & Miao, Q. M. (2007). Numerical simulation of vortex-induced vibration of a circular cylinder at low mass-damping using rans code. *Journal of Fluids & Structures*, *23*(1), 23-37. https://doi.org/10.1016/j.jfluidstructs.2006.07.007

Pantelatos, D. K., & Mathioulakis, D. S. (2004). Experimental flow study over a blunt-nosed axisymmetric body at incidence. *Journal of Fluids & Structures*, *19*(8), 1103-1115. https://doi.org/10.1016/j.jfluidstructs.2004.07.00

Peng, M., Hong-Bin, C., Lin-Fang, Q., Ren-Feng, L. I., & Gui-Gao, L. E. (2017). Numerical investigation on the effect of rotating band on aerodynamic characteristics of high-speed spinning projectile. *Acta Armamentarii 38*(12), 2363-2372 (in Chinese), https://doi.org/10.3969/j.issn.1000-1093.2017.12.009

Ren, Y. M., Wang, S. S., Li, J. W., Guo, X. C., & Mei, Y. S. (2019). Aerodynamic and trajectory characteristics of a typical mortar projectile with a deflectable nose. *Defence Technology*, *15*(5), 758-767. https://doi.org/10.1016/j.dt.2019.05.019

Richardson, E. G. (1948). The Impact of a Solid on a Liquid Surface. *Proceedings of the Physical Society*, *61*(4), 352-367. https://doi.org/10.1088/0959-5309/61/4/308

Robarge, T., Stark, A., Min, S. K., Khalatov, A., & Byerley, A. (2004). *Design considerations for using indented surface treatments to control boundary layer separation*. 42nd AIAA Aerospace Sciences Meeting and Exhibit. American Institute of Aeronautics and Astronautics. https://doi.org/10.2514/6.2004-425

Roos, F. W. (2001). Microblowing for high-angle-of-attack vortex flow control on a fighter aircraft. *Journal of Aircraft*, *38*(3), 454-457. https://doi.org/10.2514/2.2813

Seo, S. H., & Hong, C. H. (2016). Performance improvement of airfoils for wind blade with the groove. *International Journal of Green Energy*, *13*(1), 34-39. https://doi.org/10.1080/15435075.2014.910777

Sharma, G., Sharma, G., & Chopra, G. (2015). Computational and experimental study of deflected nose of missile at subsonic speed. *2015 IEEE Aerospace Conference*, 1-10. https://doi.org/10.1109/AERO.2015.7119309

Shi, Y., Hua, Y., & Pan, G. (2020). Experimental study on the trajectory of projectile water entry with asymmetric nose shape. *Physics of Fluids*, *32*(12), 122119. https://doi.org/10.1063/5.0033906

Shi, Y., Wang, G. H., & Pan, G. (2019). Experimental study on cavity dynamics of projectile water entry with different physical parameters. *Physics of Fluids*, *31*(6), 067103. https://doi.org/10.1063/1.5096588

Stutts, J., & Barrett, R. (1998). *Development and experimental validation of a barrel-launched adaptive munition*. 39th AIAA/ASME/ASCE/AHS/ASC Structures, Structural Dynamics, and Materials Conference and Exhibit. American Institute of Aeronautics and Astronautics. https://doi.org/10.2514/6.1998-2037

Thompson, K. D. (1981). *The use of a deflectable nose on a missile as a control device*. Nasa Sti/Recon Tech Rep N. https://apps.dtic.mil/sti/citations/ADA112179

Vatsa, V. N., Casalino, D., Lin, J. C., & Appelbaum, J. (2014). *Numerical simulation of a high-lift configuration with embedded fluidic actuators*. 32nd AIAA Applied Aerodynamics Conference. American Institute of Aeronautics and Astronautics. https://doi.org/10.2514/6.2014-2142

Vaughn, M., & Auman, L. (2002). *A productivity-oriented application of computational fluid dynamics to the design of a hypervelocity missile.* 20th AIAA Applied Aerodynamics Conference. American Institute of Aeronautics and Astronautics. https://doi.org/10.2514/6.2002-2937

Vaughn, M., & Auman, L. (2003). *Assessment of a productivity-oriented cfd methodology for designing a hypervelocity missile. 21st AIAA Applied Aerodynamics Conference*. American Institute of Aeronautics and Astronautics. https://doi.org/10.2514/6.2003-3937

Wang, X., Shi, Y., Pan, G., Chen, X., & Zhao, H. (2021). Numerical research on the high-speed water entry trajectories of AUVs with asymmetric nose shapes. *Ocean Engineering*, *234*, 109274. https://doi.org/10.1016/j.oceaneng.2021.109274

Wang, Y., Song, W. D., Fang, D. & Guo, Q. W. (2015). Guidance and control design for a class of spin-stabilized projectiles with a two-dimensional trajectory correction fuze. *International Journal of Aerospace Engineering*, *2015*, 1-15. https://doi.org/10.1155/2015/908304

Waugh, J. G., & Stubstad, G. W. (1975). *Hydro ballistics modeling*. Naval Undersea Center, San Diego, CA. https://apps.dtic.mil/sti/citations/ADA007529

Wauters, J., & Degroote, J. (2018). On the study of transitional low-Reynolds number flows over airfoils operating at high angles of attack and their prediction using transitional turbulence models. *Progress in Aerospace Sciences 103*, 52–68. https://doi.org/10.1016/j.paerosci.2018.10.004

Wu, Z. R., Li, M., Wang, S. L., Yang, H. Y., & Liang, X. J. (2019). Numerical research on the turbulent drag reduction mechanism of a transverse groove structure on an airfoil blade. *Engineering Applications of Computational Fluid Mechanics*, *13*(1), 1024-1035. https://doi.org/10.1080/19942060.2019.1665101

Xu, Z. Q., Liu, X. M. Liu, Y., Qin, W. X., & Xi, G. (2022). Flow control mechanism of blade tip bionic grooves and their influence on aerodynamic performance and noise of multi-blade centrifugal fan. *Energies*, *15*(9), 3431. https://doi.org/10.3390/en15093431

Yin, T. T., Jia, F. X., & Yu, J. Y. (2018). Research on roll control system for fixed canard rudder of the dual-spin trajectory correction projectile. *Wireless Personal Communications*, *103*(1), 83-98. https://link.springer.com/article/10.1007/s11277-018-5427-9

Zhang, B., Wang, S. S., Cao, M. Y., & Xu Y. X. (2014). Impacts of deflection nose on ballistic trajectory control law. *Mathematical Problems in Engineering*, *2014*, 1-6. https://doi.org/10.1155/2014/984840

Zhang, B., Wang, S. S., Cao, M. Y., & Xu Y. X. (2015). Simulation and analysis on aerodynamic characteristics of deflectable nose. *Progress in Computational Fluid Dynamics, an International Journal*, *15*(5), 279. https://doi.org/10.1504/PCFD.2015.072012